Strain accumulation and release rate in Canada: Implications for long-term crustal deformation and earthquake hazards

Adebayo Oluwaseun Ojo[1*], Honn Kao[1,2], Yan Jiang[1,2], Michael Craymer[3], and Joseph Henton[3]
[1]Geological Survey of Canada, Natural Resources Canada, Sidney, British Columbia, Canada.
[2]School of Earth and Ocean Science, University of Victoria
[3]Canadian Geodetic Survey, Surveyor General Branch, Natural Resources Canada

*Corresponding author: Adebayo Ojo (ojo.adebayo.oluwaseun@gmail.com; adebayo.ojo@canada.ca)

Key Points:

- Analysis of seismic and geodetic datasets across Canada reveals that only 20% or less of the accumulated strain is released by earthquakes
- GIA models account for most of the discrepancy between the seismic and geodetic moment rates in eastern Canada, but not in western Canada
- The recurrence time of large earthquakes (Mw ≥6) in Canada varies from decades near the plate boundary to millenniums in the plate interior

Abstract

To advance the understanding of crustal deformation and earthquake hazards in Canada, we analyze seismic and geodetic datasets and robustly estimate the crust strain accumulation and release rate by earthquakes. We find that less than 20% of the accumulated strain is released by earthquakes across the study area providing evidence for large-scale aseismic deformation. We attribute this to Glacial Isostatic Adjustment (GIA) in eastern Canada, where predictions from the GIA model accounts for most of the observed discrepancy between the seismic and the geodetic moment rates. In western Canada, only a small percentage (< 20%) of the discrepancy can be attributed to GIA-related deformation. We suspect that this may reflect the inaccuracy of the GIA model to account for heterogeneity in Earth structure or indicate that the present-day effect of GIA in western Canada is limited due to the fast response of the upper mantle to the de-glaciation of the Cordillera Ice Sheet. At locations of previously identified seismic source zones, we speculate that the unreleased strain is been stored cumulatively in the crust and will be released as earthquakes in the future. The Gutenberg-Richter (GR) model predicts, however, that the recurrence interval can vary significantly in Canada, ranging from decades near plate boundary zones in the west to thousands of years in the stable continental interior. Our attempt to quantify the GIA-induced deformation provides the necessary first step for the integration of geodetic strain rates in seismic hazard analysis in Canada.

Plain Language Summary

We took advantage of the increasing density of GNSS and seismic stations across Canada to perform a detailed investigation of the strain build-up and release rate by earthquakes. Our results indicate that strain release rates by earthquakes are slower than the strain accumulation rates except at locations where earthquakes are generated due to tectonic and/or man-made activities. We compare our results to the estimated rate of strain accumulation due to postglacial rebound and found that the postglacial rebound model can satisfactorily explain our observation in eastern Canada but not in western Canada.

Consequently, we infer that the effect of the postglacial rebound in western Canada may be short-lived or the model used is less accurate. We investigate the possibility that strain is cumulatively stored in the crust and can be released by future earthquakes. Our results reveal that the recurrence interval of a major earthquake (magnitude ≥6) can vary significantly in Canada, ranging from decades near plate boundary zones in the west to thousands of years in the stable continental interior. Our study demonstrates the advantage of jointly analyzing seismic and geodetic datasets to obtain a more complete picture of crustal deformation and potential seismic hazard.

1 Introduction

The study of seismic hazard and crustal deformation has been a common research interest for scientists in the field of seismology and geodesy. Many independent studies using either seismic data or geodetic data have been performed at different scales and resolutions in different parts of the world including Canada (e.g., Goudarzi et al., 2016; Hussain et al., 2018; Mazzotti et al., 2005). However, independent inferences from both fields are subject to different biases related to data type, inherent assumptions, processing methodologies, and measurement errors. In recent years, there have been concerted efforts to jointly analyze seismic and geodetic data to avoid the potential bias of using either dataset alone to make inferences about crustal deformation and potential seismic hazard in different tectonic settings. Hence, several studies have compared the rate of strain accumulation derived from geodetic surveys with the rate of moment released by earthquakes based on the theory of elastic rebound and the principle of moment conservation (Avouac, 2015; Barani et al., 2010; Bird et al., 2015; Grunewald & Stein, 2006; Jenny et al., 2004; Kagan, 2002; Kagan & Jackson, 2013; Mazzotti et al., 2011; Palano et al., 2018; Reid, 1910; Rontogianni, 2010; Rong et al., 2014; Ward, 1998; Walpersdorf et al. 2006). Although this involves several inherent assumptions that are debatable, this multidisciplinary approach to study crustal deformation and seismic hazard is attractive and valuable in achieving a comprehensive interpretation.

Previous studies around the world have identified inconsistent results when the seismic data are compared with the geodetic data. On one hand, agreement in the moment rate is found between the two data sets within measurement uncertainties (e.g., D'Agostino, 2014; Field et al., 1999; Kao et al., 2018; Mazzotti et al., 2011) while on the other hand, there is a disagreement between the two data sets with the geodetic moment rate typically higher than the seismic moment rate (e.g., Masson et al., 2004; Mazzotti et al., 2011; Palano et al., 2018; Ward, 1998a, 1998b). Based on the assumption of a constant rate of strain accumulation that is both elastic and inelastic and seismic moment release that is purely elastic, the degree of seismic and aseismic crustal deformation has been quantified and several factors have been invoked to explain the discrepancies between them (e.g., England & Molnar, 1997; Guest et al. 2006; Gonzalez-Ortega et al., 2018; Masson et al. 2004, 2006; Middleton et al., 2018; Palano et al., 2018; Walpersdorf et al. 2006). In the absence of aseismic deformation, areas, where the rate of geodetic strain accumulation exceeds the rate of seismic moment release, have been classified as having high potential for seismic hazard. On the other hand, areas, where the rate of seismic moment release exceeds the rate of geodetic strain accumulation, are classified as having a low potential for seismic hazard (e.g., Deprez et al., 2013; D'Agostino, 2014; Gonzalez-Ortega et al., 2018; Jenny et al., 2004; Kao et al., 2018; Keiding et al., 2015; Masson et al., 2004; Mazzotti et al., 2005, 2011; Middleton et al., 2018; Palano et al., 2018; Tarayoun et al., 2018).

In western Canada, Mazzotti et al. (2011) compared the ratios between geodetic and seismic moment rates at twelve seismic source zones and found that the geodetic and seismic moment rates only agree well within the Puget Sound and the mid-Vancouver Island seismic source zones. In most other zones classified by the authors, the geodetic moment rates are 6-150 times larger than the seismic moment rate. They attributed the differences to under-sampling of long-term moment rates by the earthquake catalogs in some zones and possible long-term regional aseismic deformation in others. The authors also investigated the possibility of integrating the geodetic strain rate into the probabilistic seismic hazard analyses (PSHA) and concluded that it led to an overestimation of the ground shaking estimates. In studying the seismogenesis of induced seismicity in western Canada, Kao et al. (2018) also compared the geodetic moment rate to seismic moment rate and found close agreement in the injection-induced earthquake dominated regions.

Most of these previous studies have noted that the comparison of geodetic and seismic moment rates suffers significantly from the lack of dense Global Navigation Satellite System (GNSS) station coverage and the short duration of recordings and this has been reported to possibly contribute to the observed imbalance between the two moment rate estimates. Likewise, the unavailability of long earthquake catalogs that spans the recurrence interval of large magnitude earthquakes also leads to a high probability of underestimating the long-term seismic hazard (Ward, 1998; Mazzotti et al., 2011; Pancha et al., 2006). However, in the past decade, there has been a significant increase in the number of available public and private continuously operating GNSS stations all over Canada (e.g., the Real-Time Kinematic (RTK) Networks) in addition to the scientific advancement in efficient processing techniques (e.g., Blewitt et al., 2018). Similarly, more broadband seismic stations have been deployed across the country and robust earthquake detection algorithms have been developed (e.g., Dokht et al., 2019; Tan et al., 2019). This makes it possible to significantly reduce the uncertainties associated with the GNSS velocities and strain rate estimates and to build improved seismic catalogs with robust moment magnitudes estimates (e.g., Atkinson et al., 2014; Moratto et al., 2017; Visser et al., 2017). Therefore, in this study, we seek to improve upon the previous investigations of crustal deformation and associated processes in western Canada (e.g., Mazzotti et al., 2011) by using data from a denser GNSS station coverage and a more complete earthquake catalog. Also, for the first time, we extend this multidisciplinary approach to study crustal deformation in central and eastern Canada. In these regions, both the ongoing post-glacial rebound (PGR) induced strain and numerous intraplate earthquakes provide the opportunity to robustly constrain the seismic versus aseismic partitioning of long-term deformation (Mazzotti et al., 2005; Tarayoun et al., 2018). Additionally, we approach the computation and subdivision of the study area differently, to obtain a spatial variation of the moment rates across the study region. While our study confirms previous observations, the newly developed deformation-rate models have unprecedented resolution and provides new insights into crustal deformation and earthquake hazards in Canada.

2 Seismic Hazard in Canada

Large magnitude earthquakes have occurred in and around Canada in the past and will certainly continue to occur sometimes in the future (Cassidy et al., 2010; Neely et al., 2018). Meanwhile, non-destructive small-magnitude earthquakes are recorded continuously by broadband seismic stations across the country (see Figure 1a). Qualitative analyses of the spatial distribution of these earthquakes reveal a strong correlation between their epicenters and the locations of densely populated urban centers and known tectonics structures (Cassidy et al., 2010; Figure 1). For instance, there is a concentration of relatively large and frequent earthquakes surrounding the Cascadia Subduction Zone (CSZ) where the oceanic Juan de Fuca and Explorer plates are subducting beneath the North American plate (NA) at an estimated rate of 2−5 cm/yr (Riddihough & Hyndman 1991; Gao et al., 2017; Yousefi et al., 2020). The M7.3 event on central Vancouver Island in 1946 is an example of large crustal earthquakes in this region. Similarly, in the northern part of the west coast, the oceanic Pacific plate and the NA slide past each other along the seismically active Queen Charlotte Fault (QCF) where the M8.1 earthquake occurred in 1949. In the St. Elias region of southwest Yukon Territory, the Yakutat Block (YB) subducts beneath NA to the northeast leading to fast mountain building with significant seismicity. Moving inland from the Pacific Coast, the Canadian Cordillera which accommodates the crustal stress transferred inland from the subduction zone is characterized by a relatively high level of seismicity especially in the northern Rocky Mountain region (Cassidy & Bent 1993; Chen et al., 2018; Mazzotti & Hydnman, 2001). Farther inward in the interior platforms, the rate of seismicity decreases in the stable Craton and sedimentary plains. However, there are reports of increasing induced seismicity associated with mining and hydraulic fracturing for oil and gas exploration in the southern part of this region (e.g., Kao et al., 2018; Figure 1a).

In contrast, eastern Canada is in the stable interior of NA. The reactivation of tectonic structures (e.g., failed rifts, impact crater, and old faults) in zones of crustal weakness by regional stress fields and the ongoing glacial isostatic adjustment (GIA) causes numerous intraplate earthquakes to occur in the region (George et al., 2011; Lamontagne, 1999; Lambert et al., 2001; Mazzotti et al., 2005; Mazzotti & Townend, 2010; Park et al., 2002; Sella et al., 2004; Tiampo et al., 2011; Tarayoun et al., 2018). During the last glacial maximum (LGM), the thick (~ 3 km) Laurentide Ice Sheet (LIS) that covered most parts of eastern Canada depressed the lithosphere and caused the peripheral to bulge due to viscoelastic flow in the mantle. However, due to deglaciation, the lithosphere is rebounding while the peripheral bulges are migrating downward, causing a three-dimensional (3D) movement of the Earth's crust measurable by GNSS and accompanied by a perturbation to the geoid (Sella et al., 2007; Simon et al., 2016; Henton et al., 2006; Lavoie et al., 2012; Mitrovica et al., 2001; van der Wal et al., 2009; Wahr et al., 1995). This ongoing GIA process is well constrained by geodetic measurements which revealed pictures of GIA-induced uplift all over eastern Canada with a maximum rate of 13.7 ± 1.2 mm/yr around the south-eastern part of the Hudson Bay and subsidence with a minimum rate of −2.7 ± 1.4 mm/yr to the south of the St. Lawrence River Valley (SLRV) (Dyke, 2004; Goudarzi et al., 2016; Henton et al., 2006; Lamothe et al., 2010; Mazzotti et al., 2005; Peltier, 1994, 2002; Sella et al., 2007; Tushingham & Peltier, 1991). Many years of seismic recordings in this region have revealed clusters of earthquake activities (i.e. seismic source zones) along the St. Lawrence River and the Ottawa valley which includes the western Quebec seismic zone (WUQ), the Charlevoix Seismic Zone (CHV), and the Lower Saint Lawrence Seismic Zone (LSZ) (Lemieux et al., 2003; see Figure 1). Five earthquakes greater than M6 occurred in CHV between 1663 and 1925 and the region on average has more than 200 earthquakes annually, making it the most seismically active region in eastern Canada. Likewise, four earthquakes larger than M5 occurred in the WUQ in the past three centuries. Other identified seismic zones include Northeastern Ontario (NON), the Southern Great Lakes

(SGL), the Northern Appalachians (NAP), and the Laurentian Slope (LSP) where a magnitude M7.2 earthquake occurred in 1929 (see Figure 1).

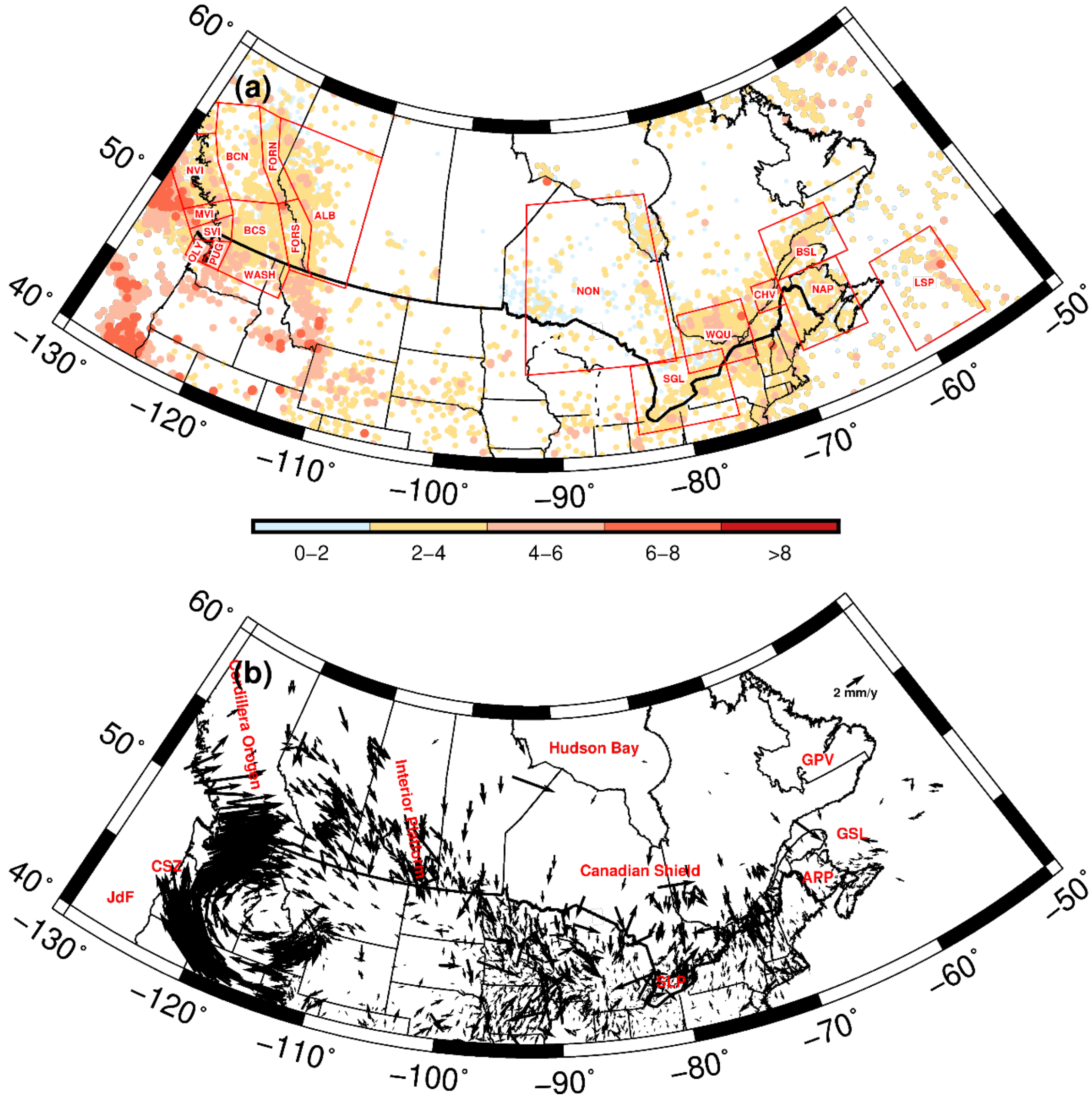

Figure 1. (a) Epicentre distribution of earthquakes (>45,000 events in total) in the newly compiled catalog. Red boxes indicate the location of previously defined seismic source zones in the region namely: NVI - North Vancouver Island-South Queen Charlotte; FORN - Foreland Belt-North; FORS - Foreland Belt-South; ALB - Alberta Plains; BCN - Central British Columbia-North; BCS - Central British Columbia-South; MIV - Mid Vancouver Island; WASH - Northeast Washington; SVI - South Vancouver Island; PUG - Puget Lowland; OLY - Olympic Mountains; NON - Northeastern Ontario; SGL - Southern Great Lakes; WQU - Western Quebec; CHV - Charlevoix-Kamouraska; BSL - Lower St. Lawrence; NAP - Northern Appalachians and LSP - Laurentian Slope. (b) Horizontal GNSS station velocities relative to the stable North America reference frame after inter-seismic correction at the plate boundary zone. For a clearer view, we did not plot the error ellipse (most sites ≤ 1 mm/yr) but it is included in Table S1. The data length for each station is greater

than 3 years. Locations of the main tectonic features in Canada are noted including the Cordillera Orogen; the Interior Platform (e.g., Western Canada Sedimentary Basins); CSZ: Cascadia Subduction Zone; JdF: Juan de Fuca Plate; Hudson Bay Platform; Canadian Shield; GSL: Gulf of St. Lawrence; APP: Appalachian Orogen, SLP: St. Lawrence Platform, and GPV: Grenville Platform.

3 Data and Methodology

3.1 Earthquake Catalog

In this study, we use a seismic catalog containing 45,114 earthquake events spanning over 486 years with reliable moment magnitude estimates. We obtained this by a careful compilation of novel and published seismic catalogs encompassing most of western, central and eastern Canada in addition to the Northern part of the contiguous United States (see Figure 1; Table S2). The bulk of the dataset came from the published 2011 Canadian Composite Seismicity Catalogue (Fereidoni et al., 2012) which includes both historical and instrumentally recorded earthquakes with homogenized moment magnitude estimates compiled from several sources (e.g., Adams & Halchuk, 2003; Petersen et al., 2006; Ristau, 2004). We also include more recent earthquake records from the Composite Alberta Seismicity Catalogue (CASC) which includes earthquakes in Alberta and northeastern British Columbia with moment magnitudes from different agencies (Cui & Atkinson, 2016; Fereidoni & Cui, 2015; Novakovic & Atkinson, 2015; Stern et al, 2013). To increase the number of small magnitude earthquakes included in the study, we compute moment magnitudes for about 16,000 small magnitude earthquakes ($M \leq 4$) contained in the Natural Resources Canada's (NRCan) online catalog and the earthquake catalog of Visser et al. (2017) using the Pseudo Spectral Acceleration (PSA) method of Atkinson et al. (2014). We identified and removed duplicate entries (i.e., earthquakes that are closely placed in time and location) to produce a unique comprehensive earthquake catalog. Overall, there are few earthquakes with moment magnitude ≥ 6 (~ 198 events) but we did not include the M9 Cascadia Megathrust Earthquake on January 26, 1700, to remove potential bias in our comparative analysis since we modeled and removed the effect of inter-seismic subduction zone strain buildup along the CSZ.

3.2 Seismic Moment Rate Estimate

To quantify the elastic strain release rate, we estimate the seismic moment rate using both the Kostrov summation (Kostov, 1974) and the truncated Gutenberg-Richter (GR) distribution method (Kao et al., 2018). Estimates based on the Kostrov summation method is computationally straightforward but known to suffer significantly from an incomplete seismic catalog. In comparison, the GR method involves more steps but has the advantage of being insensitive to the length of the earthquake catalog. For all computations, we subdivided the study area into a 2° x 2° grid that provides a consistent data set across the study area (e.g., Ghofrani & Atkinson, 2016; Gutenberg & Richter, 1944; Kao et al., 2018; Kostrov, 1974; Palano et al., 2018). We followed a numerical approach to estimate the seismic moment rate based on the GR method (Kao et al., 2018). First, we estimate the magnitude of completeness (M_c) and associated uncertainty from 10^4 Monte Carlo simulations using the maximum curvature method of Wiemer (2000) with a magnitude bin width of 0.25 (see Figure S1). We adopt this technique because it is fast and has the advantage of achieving a stable result even with few events like we had for many of the computation grid (Mignan et al. 2011; Mignan & Woessner, 2012). Subsequently, we estimated the earthquake a and b-value parameters alongside their standard errors using both the maximum likelihood estimation method (Aki, 1965; Weichert, 1980) and the least square regression method. To avoid overfitting for the linear least-squares regression, we searched for the data window that provides optimum a and b values (i.e. smallest error values) between M_c and the maximum observed magnitude. We also attempt to estimate the earthquake a-values and b-values using the maximum likelihood estimation method (Aki, 1965; Weichert, 1980). Where both methods are successful, we use the MLE estimate and augment with an estimate from LSQ where it is successful and there is no MLE estimate. We obtained the maximum possible earthquake magnitude (M_{max}) from the 2015 Canadian Seismic Hazard Model (Halchuk et al., 2015). Using the earthquake parameters (i.e., Mc, M_{max}, a, and b values) estimated for each grid, we compute the total amount of seismic moment for each magnitude bin from M_c up to M_{max} and divide the sum by the catalog duration (T) to derive the yearly seismic moment rate from the G-R distribution:

$$\dot{M}_0^{SG} = \frac{1}{T}\sum_{i=M_c}^{M_{max}} \left(10^{\frac{a-bi}{a-b(i+s)}}\right) \times \left(10^{1.5(i+6.03)}\right) \tag{1}$$

where i indicates different earthquake magnitude ranging from M_c to M_{max} and s is the magnitude increment or step. The first term in the summation is the number of events derived from the G-R distribution while the second term converts the event magnitude to seismic moment following the formulation of hanks and Kanamori (1979). To obtain upper, and lower bound estimates for the seismic moment rates ($\dot{M}_0^{SG}$) in each cell, we vary the input parameters based on the estimated standard errors (i.e. a: a/a-σ/a+σ; b: b/b-σ/b+σ for the median, minimum and maximum estimates) similar to previous studies (e.g., Mazzotti et al., 2011; Palano et al., 2018).

An alternative method that is commonly used to estimate the seismic moment rate is provided by Kostrov (1974). In this method, the seismic moment rate for the total number of earthquakes (N) occurring in a volume (V) is simply calculated by summing the moment of the individual earthquakes normalized by the catalog period in each grid (T) (Ward, 1998a, 1998b). We use the formula of Hanks & Kanamori (1979) to convert the earthquake moment magnitude (M_w) obtained from the catalog to scalar seismic moment (M_0) and we estimate the seismic moment rate as follows:

$$\dot{M}_0^{SK} = \frac{1}{T}\sum_{i=n}^{N} \left(10^{1.5(M_w+6.03)}\right)^n \tag{2}$$

The moment magnitude estimates for each event came from different sources and derived from methods such as regression analysis and conversion formulas that are susceptible to errors. Hence, we estimate an upper and lower bound for the $\dot{M}_0^{SK}$ by propagating a maximum standard error of ±0.2 magnitude unit on the moment magnitude estimates (e.g., Castellaro et al., 2006; Ristau et al., 2005).

3.3 GNSS Data Processing

The GNSS observation data used in this study came from different operators (e.g., commercial, national and provincial networks) and includes more than 3000 continuous and campaign stations deployed throughout Canada and the adjacent U.S. (e.g., Kreemer et al., 2014, 2018; see Figure 1b; Table S1). We started by processing the RINEX data recorded by ~1000 Real-Time Kinematic (RTK) receivers and obtained daily three components position time-series by following the same procedure described in Kao et al. (2018) (e.g., Blewitt et al., 2013; Kreemer et al., 2014). Specifically, we used the GIPSY v6.4 software package provided by the Jet Propulsion Laboratory (JPL) to process the raw RINEX data following a standard precise point positioning method (Zumberge et al., 1997). We use the Wide Lane Phase Bias method of Bertiger et al. (2010) to resolve the phase ambiguity and determine the final station coordinates under the IGS14 realization of the ITRF2014 reference frame (Altamimi et al., 2016).

We estimate the GNSS station velocities and associated uncertainties using the robust Median Interannual Difference Adjusted for Skewness (MIDAS) software available from the Nevada Geodetic Laboratory (NGL) (Blewitt et al., 2016). Our preference of the MIDAS algorithm is mainly because it can better handle common problems such as step discontinuities, outliers, skewness, and heteroscedasticity (Blewitt et al., 2016; Sen, 1968; Theil, 1950). To enhance the density of the GNSS station coverage across Canada, we included horizontal velocities in the ITRF2014 frame from the online database of NGL (Blewitt et al., 2018) and JPL. To emphasize the deformation across Canada, we transformed the combined velocity fields using the ITRF2014 rotation for the North American Plate (Altamimi et al., 2017). For stations common to the three sources (i.e. this study, NGL, and JPL), we retain our velocity estimates while we adopt the velocities from the NGL database for most stations and only use velocities of stations unique to the JPL database. To ensure the stability and quality of our result, we remove GNSS stations with velocities estimated from time-series records for less than 3 years (Blewitt & Lavallée, 2002). Likewise, we modeled and removed the inter-seismic strain accumulation due to the locking of the Queen Charlotte Fault and subduction faults in the Cascadia and the Haida Gwaii subduction zones from the original velocity estimates (e.g., Kao et al., 2018; Mazzotti et al., 2003; Wang et al., 2003). Finally, we are left with ~2250 reliable horizontal GNSS station velocities shown in Figure 1(b) and presented in Table S1.

3.4 Geodetic Moment Rate Estimate

We use the GNSS horizontal velocities to compute the regional strain field and associated standard error over the study area on a regular 0.5° × 0.5° grid following the method of Shen et al. (2015). This method employs a weighted least squares approach to interpolate the GNSS horizontal velocity field and computes the strain rate at a resolution that depends on the in-situ data strength. Since we are primarily interested in regional strains, we searched for the optimum spatial smoothing parameter (D) using a quadratic weighting function from 1 km to 500 km at an interval of 1 km with a threshold weight (Wt) of 24 after several tests. Subsequently, we compute the geodetic moment rate at each 0.5° x 0.5° grid space and then integrate over the larger 2° × 2° grid using the formula of Savage and Simpson (1997):

$$\dot{M}_0^G = 2\mu H_s A[Max(|\varepsilon_{H\,max}|, |\varepsilon_{h\,min}|, |\varepsilon_{H\,max} + \varepsilon_{h\,min}|)] \quad (3)$$

where μ is the shear modulus of the rocks, H_s is the seismogenic thickness, A is the area, ε_{Hmax} and ε_{hmin} are the principal axes of the computed horizontal strain rate. Since the focal depths of the earthquakes are not well constrained, we use one-third of the crustal thickness estimated from the Canada-wide ambient seismic noise tomography study of Kao et al. (2013) to approximate the seismogenic thickness (H_s) at each grid. Rather than the commonly used homogeneous fixed value, this approach helps us to reflect the variation in the seismogenic thickness across the study area (e.g., Mazzotti et al., 2011; Middleton et al., 2018). Finally, we estimate the median, minimum and maximum geodetic moment rate in each 2° x 2° grid by varying the input parameters in Equation 3 (i.e., μ: 3E+10/2.5E+10/3.5E+10; H_s: H_s/ H_s-2/ H_s+2 and ε: ε/ε-σ/ ε+σ) (e.g., Mazzotti et al., 2011).

4 Results

Although our analysis extends into the northern part of the U.S., we primarily focus on the results obtained within the Canadian landmass. Hence, results to the south of the Canada–USA border will mostly be ignored in subsequent discussions. Based on the spatial distribution of earthquakes and GNSS station coverage, our results are best constrained in the south-eastern and the south-western part of the study area (see Figure 1).

Considering the tectonic, geological, and geodetic characteristics, Mazzotti et al. (2011) divided western Canada into twelve seismic source zones. We adopt their classification and compute earthquake parameters and moment rate estimates at eleven of these seismic source zones, including (1) NVI - North Vancouver Island-South Queen Charlotte; (2) FORN - Foreland Belt-North; (3) FORS - Foreland Belt-South; (4) ALB - Alberta Plains; (5) BCN - Central British Columbia-North; (6) BCS - Central British Columbia-South; (7) MIV - Mid Vancouver Island; (8) WASH - Northeast Washington; (9) SVI - South Vancouver Island; (10) PUG - Puget Lowland and; (11) OLY - Olympic Mountains (see Fig. 1a). Similarly in eastern Canada, we followed the seismic source zone classification provided by the Natural Resources Canada, namely: (1) NON - North-eastern Ontario; (2) SGL - Southern Great Lakes; (3) WQU - Western Quebec; (4) CHV - Charlevoix-Kamouraska; (5) BSL - Lower St. Lawrence; (6) NAP - Northern Appalachians and; (7) LSP - Laurentian Slope (see Fig. 1a). In this study, we performed two sets of computations. First, we divided the entire study region into a 2° x 2° grid and estimate the geodetic and the seismic moment rates (see Sections 3.2 and 3.4) at each grid. Since this approach is unique to our study, we performed a second set of computations following the seismic zone approach to compare our results with previous studies. Hence, for each of the aforementioned seismic source zones in western and eastern Canada, we estimated a representative value for the geodetic and seismic moment rates. We present the results obtained for the regular grids and each seismic source zone independently in sections 4.2 and 4.3, respectively, and we only compare the result at specific seismic source zones (section 4.3) to other studies.

4.1 GNSS Velocity and Strain Rate Field

The final set of GNSS horizontal velocities relative to the stable North American plate is shown in Figure 1b. The GNSS horizontal velocities are estimated from time series ranging from 3 to 26 years (average of 9.3 years) and the amplitudes range of 0.01–6.9 mm/yr with a standard error of 0.2–1 mm/yr (see Table S1). Besides the obvious clockwise block rotation observed at GNSS stations located in the pacific northwest, most station velocities are pointing in the NE–SW direction along the Cascadia subduction zone (Figure 1b). In the Cordillera region and the inner platform, most of the GNSS station velocities reveal a coherent NW–SE regional gradient. In eastern Canada, the velocities are generally oriented NW–SE but the pattern near the margins of the formal glaciated areas are quite complex and incoherent. However, relatively large velocity amplitudes can also be seen along the St. Lawrence River valley in agreement with previous studies (e.g., Goudarzi et al., 2016; Lamothe et al., 2010; Mazzotti et al., 2005; Tarayoun et al., 2018; see Figure 1b).

Figure 2a presents the interpolated 2-D strain rate field derived from the horizontal velocities and shows the principal extensional and contractional strain rate at each 0.5° x 0.5° grid point. In general, the main feature in the strain rate tensor agrees well with previous studies (e.g., Alinia et al., 2017; Argus & Peltier, 2010; Calais et al., 2006; George et al., 2012; Goudarzi et al., 2016; Kreemer et al., 2018; Kao et al., 2018; Mazzotti et al., 2011; Park et al., 2002; Peltier et al., 2015; Sella et al., 2007; Snay et al., 2016; Tiampo et al., 2011; Tarayoun et al., 2018) indicating the robustness of our strain rate computation. The strain rate field is interpolated across the study region to obtain a finer resolution in regions with relatively sparse GNSS stations and to emphasize regional-scale deformation. However, the strain rate result is clipped at the peripheral of the study region where the sparsity of GNSS station does not allow for the strain rate to be reliably resolved (see Figure 2a). The maximum ($\dot{\varepsilon}_1$) and minimum ($\dot{\varepsilon}_2$) principal components of the computed strain rate tensors range from -1.9 to 19.6 nstrain/yr and -17 to 3.3 nstrain/yr, respectively while the associated error range from 0.1 – 3.2 nstrain/yr and 0.1 – 3.6 nstrain/yr, respectively (Figure 2a and b). We note that the estimated strain rate error is not particularly larger at locations where the GNSS station is sparse (Figure 2b) but further Monte Carlo simulations indicate that they are not well constrained like estimates at locations of relatively dense GNSS stations (Figure S2 and S3). Although, the maximum shear strain rates can be up to 10.5 nstrain/yr in the study region, for most of the study region the maximum shear strain rate is within 2 nstrain/yr (where nstrain = 10e^{-9}). We compute the style of the strain rate tensor, i.e., the areal strain rate defined as $\left(\frac{\dot{\varepsilon}_1 + \dot{\varepsilon}_2}{max(|\dot{\varepsilon}_1|,|\dot{\varepsilon}_2|)}\right)$, to reveal the differences in the strain rate magnitude across the study region (e.g., Kreemer et al., 2014; 2018; see Figure 2b). The scale is saturated at -1 and +1 to clearly show when both principal axes are either compressional or extensional (Figure 2b). The main features include a pronounced extensional strain rate to the east of Hudson Bay and the Grenville Platform bounded by contractional strain rate on its margins. A band of substantial contractional strain rate (~ 4 nstrain/yr) between latitudes 40°N and 50°N centered around 85°W follows the St. Lawrence Platform and the Canada-US boundary (Figure 2). To the far east, this band lies between the extensional strain rate in Hudson Bay to the north and a more dispersed extensional strain rate to the south within the Appalachian (see Figure 2b). Predominant contractional strain rate trending SW–NE is observed along the Pacific Coast and Vancouver Island and the amplitude decreases with minor shortening within the Cordillera region (e.g., Snay et al., 2016). A localized extensional strain rate can also be seen in the northern interior platform and to the west of Hudson Bay (Figure 2b; Calais et al., 2016; Goudarzi et al., 2016). However, large uncertainties exist at locations where the GNSS station coverage is relatively sparse, and a more constrained result may only be achieved in the future with denser networks and longer data collection (see Figure 1b).

4.2 Moment Rate Estimates across the 2° x 2° grids

In this section, we present the result of moment rate estimates at each 2° x 2° grid. The estimated geodetic and seismic moment rates are presented in Figure 3 and Table S3. Although these maps confirm some first-order features reported by previous estimations, it presents a holistic result across the western and eastern parts of Canada with some new observations. The magnitude of the geodetic moment rate ($\dot{M}_0^G$)

(Figure 3a) ranges from 4.5×10^{15} to 4.0×10^{17} Nm/yr and the estimated error from bootstrapping ranges from $0.01 – 0.5 \times 10^{17}$ Nm/yr (Figure S3).

Figure 3a shows two patterns of strain rate accumulation. Most of the study area is characterized by strain accumulation in the range of $10^{16} – 10^{17}$ Nm/yr. In this interval, we observe the lowest rates of strain accumulation ($\leq 5 \times 10^{16}$ Nm/yr) within the Hudson Bay, the western Canadian Shield, and some locations in the Appalachian and the Gulf of St. Lawrence (Table S3). However, we cannot rule out the possibility that these low strain rate values may be related to the lack of in-situ observation at these locations (see Figure 1b) and new features may emerge when such observation gaps are filled in the future. Regions with a relatively higher rate of strain accumulation (5×10^{16} - 10^{17} Nm/yr) are mainly located along the St. Lawrence River Valley and the Interior Platform (Figure 3a).

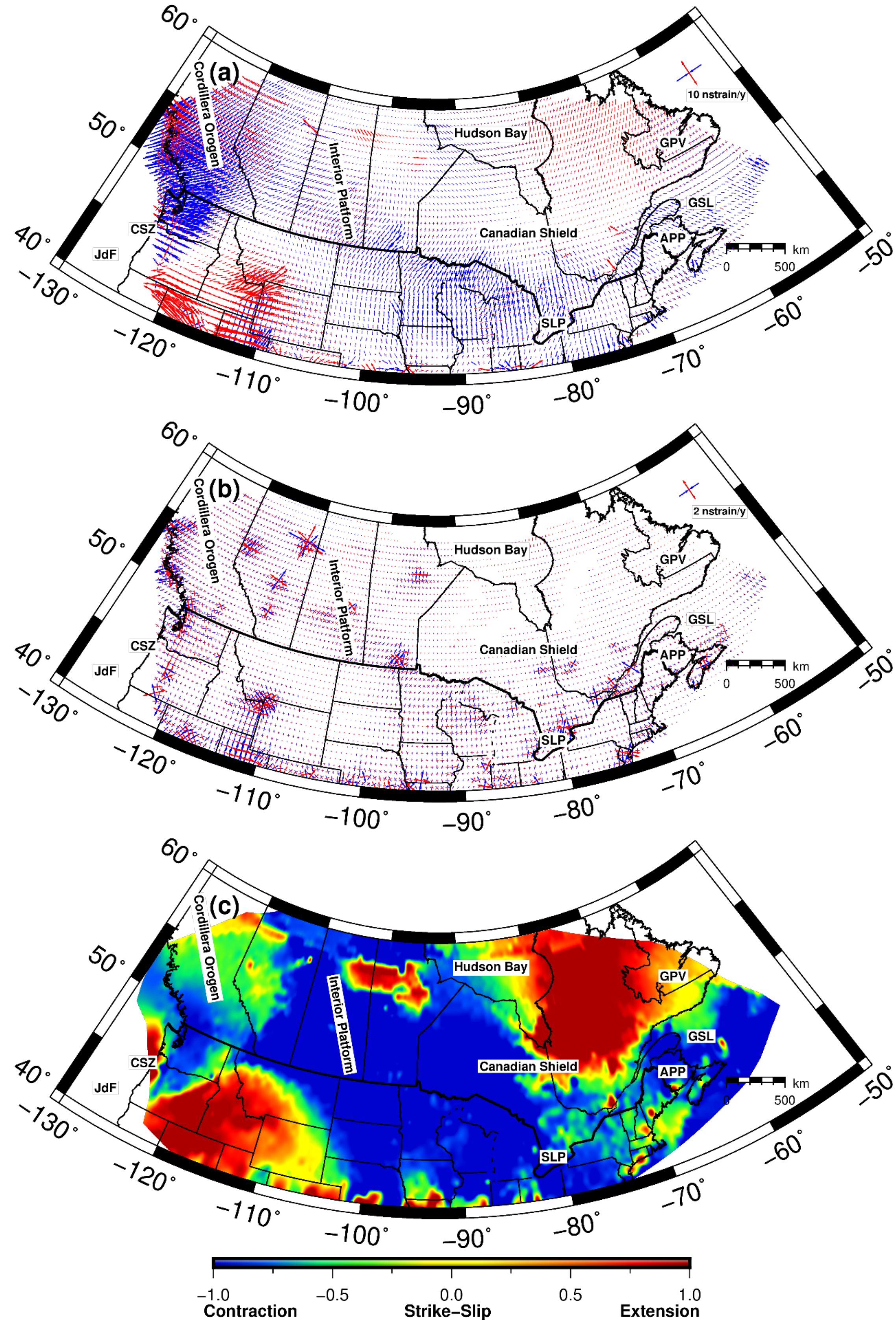
(a)
(b)
(c)
Cordillera Orogen
Interior Platform
Hudson Bay
Canadian Shield
GPV
GSL
APP
SLP
CSZ
JdF
10 nstrain/y
2 nstrain/y
km
0
500
60°
50°
40°
−130°
−120°
−110°
−100°
−90°
−80°
−70°
−60°
−50°
−1.0
−0.5
0.0
0.5
1.0
Contraction
Strike−Slip
Extension

Figure 2. (a) The smoothed horizontal strain rate field and (b) associated error at a grid spacing of 0.5° x 0.5° across the study area. The red and blue crosses indicate the orientation and magnitude of the extensional and contractional strain rate, respectively. (c) Style of strain rate tensor is defined by Kreemer et al. (2014). The scale ranges from -1 when both principal axes are compressional to +1 when both principal axes are extensional. The main geological and tectonic features in the study area and abbreviations are the same as in Figure 1.

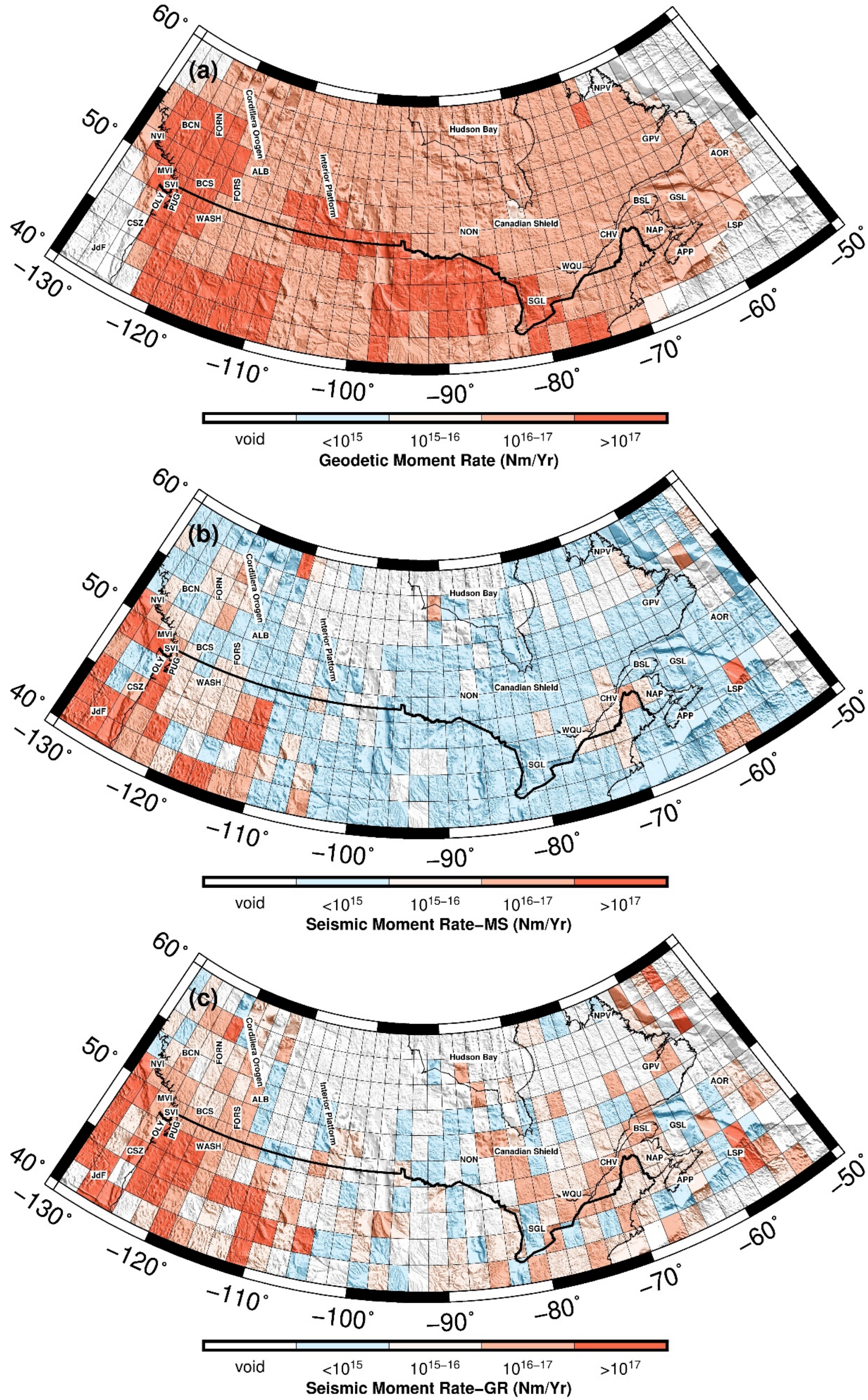
(a)
Cordillera Orogen
Interior Platform
Hudson Bay
Canadian Shield
BCN
FORN
NVI
MVI
SVI
OLY
PUG
BCS
FORS
ALB
CSZ
WASH
JdF
NON
NPV
GPV
AOR
BSL
GSL
CHV
NAP
LSP
APP
WQU
SGL
60°
50°
40°
−130°
−120°
−110°
−100°
−90°
−80°
−70°
−60°
−50°
void
<10^{15}
10^{15-16}
10^{16-17}
>10^{17}
Geodetic Moment Rate (Nm/Yr)
(b)
Seismic Moment Rate−MS (Nm/Yr)
(c)
Seismic Moment Rate−GR (Nm/Yr)

Figure 3. Estimates of the moment rates in each 2° x 2° grid from (a) geodetic data (b) earthquake data using the cumulated Kostrov summation method (c) earthquake data using the truncated Gutenberg-Richter distribution method. The upper and lower bound of the estimates are presented in Table S3. The locations of existing seismic source zones and the main tectonic features in the study area are shown on the maps and defined in Figure 1. The thick black line defines the Canada-US border to the south.

The rate of strain accumulation ranges from 1.0 to 1.5 × 10^{17} Nm/yr along the Canada-USA border and coincides with a band of localized high contractional strain rates (e.g., Goudarzi et al., 2016; see Figure 2a). The most significant rates of strain accumulation (≥10^{17} Nm/yr) are observed within the Canadian Cordillera with increasing magnitude into the Cascadia subduction zone where the North American, Pacific, and Juan de Fuca plates interact (Figure 2a).

The moment release rate estimated by summing the seismic moment of individual earthquakes in the catalog normalized by the catalog duration ($\dot{M}_0^{SK}$) and that obtained by integrating the cumulative truncated Gutenberg-Richter distribution up to an assumed maximum magnitude ($\dot{M}_0^{SG}$) follow the same variation pattern across the different tectonic regions (Figures 3b and 3c). The $\dot{M}_0^{SK}$ ranges between 10^{11} and 5.1 × 10^{18} Nm/yr while the $\dot{M}_0^{SG}$ ranges between 2.0 × 10^{12} and 3.3 × 10^{18} Nm/yr across the study area (Figures 3b and 3c). For ~91% of the grid points, the values of $\dot{M}_0^{SK}$ is smaller than the $\dot{M}_0^{SG}$ estimates with a ratio between 10^{-6} and 0.98 (e.g., Deprez et al., 2013; Mazzotti et al., 2011). The observed differences can be attributed to the inherent limitations of the two seismic moment rate estimation methods. The $\dot{M}_0^{SK}$ estimates (Figure 3b) relied essentially on observation (known events in the catalog) while the $\dot{M}_0^{SG}$ estimates (Figure 3c) used the distribution of known events to model possible missing large magnitude earthquakes and include them in the moment rate estimation. This can be well observed in central and eastern Canada where the two models have more obvious discrepancies due to lack of events and a larger number of small magnitude events that contribute relatively small moments. However, along the west coast, where our catalog is more complete and we have relatively large magnitude earthquakes, the seismic moment rate models agree better. The spatial distribution of strain release rate reveals that the rate of seismic moment release is the lowest ($\dot{M}_0^{SK}$ ≤10^{15} N.my/r) in the Interior Platform, the Hudson Bay, the Canadian Shield, the Grenville, and in the Gulf of St. Lawrence. The limited number of earthquakes in these regions did not allow for a successful estimate of the earthquake parameters (i.e., the a and b values) needed for the $\dot{M}_0^{SG}$ computation (void grids in Figure 3c). We observe an intermediate rate of seismic moment release (between 10^{16} and 10^{17} Nm/yr) within the Cordillera (e.g., ALB, FORN, FORS, BCN, BCS in Figures 3b and 3c) and along the St. Lawrence River Valley in eastern Canada (e.g., SGL, WQU, CHV, BSL and NAP in Figures 3b and 3c). The highest rates of seismic moment release (≥ 10^{17} Nm/yr) are found along the seismically active Cascadia subduction Zone (e.g., NVI, SVI, OLY, PUG, and WASH) and within the LSP seismic source zone in eastern Canada (see Figures 3b and 3c).

4.3 Moment Rate Estimates at Specific Seismic Source Zones

In this section, we summarize the results obtained for each of the seismic source zones in western and eastern Canada (see Figure 1a and Table 1). Table 1 shows that the newly compiled earthquake catalog contains 129 to 9471 earthquakes recorded over 101 to 486 years in the seismic source zones as compared to 11 to 122 earthquakes spanning over 50 - 100 years used in the study of Mazzotti et al. (2011) in western Canada (see Table 1). The maximum observed earthquake magnitude in each source zone ranges from M4.7 to M7.3 and is generally smaller than the expected maximum earthquake magnitude (M_{max}) from the 2015 Canadian Seismic Hazard Map which ranged from M7.2 to M7.9 (Halchuk et al., 2015). The b values indicating the proportion of small to large magnitude earthquakes in each seismic source zone range from 0.58 to 0.99 while the seismicity levels (i.e., the a-values) range between 4.17 and 5.91.

Table1: Earthquake parameters and moment rate estimates at specific seismic source zones in Canada

Seismic Source zones	Earthquake Parameters						$\dot{M}_0^G$ (10^{11} Nm/km²/Yr)			Strain Rate	$\dot{M}_0^{SK}$ (10^{17} Nm/Yr)			$\dot{M}_0^{SG}$ (10^{17} Nm/Yr)		
	N	T(Yrs)	Mx	b-value	a-value	Mc	Estimate	Lower	Upper	(nstrain/y)	Estimate	Lower	Upper	Estimate	Lower	Upper
ALB	9471	219	7.7	0.99 ± 0.04	5.91 ± 0.15	1.75 ± 0.01	0.70	0.42	1.08	1.28	0.14	0.07	0.29	0.62	0.23	1.67
BCN	2527	101	7.3	0.88 ± 0.03	5.35 ± 0.15	2.00 ± 0.46	1.76	1.14	2.55	3.52	0.32	0.16	0.65	1.14	0.50	2.60
BCS	2579	113	7.5	0.78 ± 0.03	4.84 ± 0.13	1.50 ± 0.44	4.10	2.68	5.90	2.78	0.25	0.13	0.50	1.74	0.79	3.87
FORN	4553	101	7.2	0.91 ± 0.04	5.28 ± 0.16	1.75 ± 0.05	2.76	1.77	4.04	2.48	0.29	0.15	0.59	0.58	0.22	1.58
FORS	3811	101	7.4	0.99 ± 0.04	5.72 ± 0.16	2.00 ± 0.07	2.68	1.74	3.89	1.56	0.21	0.11	0.42	0.59	0.22	1.59
MVI	9094	155	7.3	0.74 ± 0.04	5.38 ± 0.13	2.00 ± 0.19	10.19	6.66	14.70	4.56	18.75	9.40	37.42	6.16	2.56	14.83
NVI	6118	102	7.3	0.72 ± 0.03	5.46 ± 0.10	2.50 ± 0.13	3.90	2.51	5.69	5.11	21.84	10.95	43.58	14.25	7.57	26.82
OLY	5842	160	7.5	0.60 ± 0.02	4.67 ± 0.06	1.50 ± 0.01	11.81	7.62	17.23	4.27	16.97	8.50	33.85	11.81	7.58	18.40
PUG	5382	160	7.6	0.58 ± 0.01	4.58 ± 0.04	1.50 ± 0.01	15.81	10.28	22.89	4.85	10.54	5.28	21.03	16.60	12.88	21.39
SVI	5902	155	7.5	0.73 ± 0.02	4.92 ± 0.08	1.50 ± 0.01	14.25	9.32	20.52	4.31	6.86	3.44	13.69	3.33	2.08	5.36
WASH	2404	128	7.6	0.80 ± 0.05	5.14 ± 0.21	2.00 ± 0.23	3.18	2.03	4.67	2.12	0.15	0.08	0.31	2.67	0.77	9.28
BSL*	839	342	7.9	0.93 ± 0.04	4.79 ± 0.15	2.00 ± 0.04	1.29	0.81	1.92	0.82	< 0.01	<< 0.01	< 0.01	0.11	0.04	0.28
CHV*	1343	485	7.8	0.79 ± 0.02	4.53 ± 0.08	2.00 ± 0.25	3.59	2.08	5.68	0.97	0.10	0.05	0.20	0.30	0.18	0.48
LSP*	219	126	7.9	0.73 ± 0.06	4.17 ± 0.27	2.75 ± 0.20	0.27	0.16	0.41	0.73	5.58	2.79	11.12	1.57	0.32	7.66
NAP*	1012	264	7.6	0.80 ± 0.02	4.59 ± 0.08	2.00 ± 0.03	0.83	0.49	1.30	0.86	0.13	0.07	0.26	0.36	0.21	0.60
NON*	725	125	7.8	0.94 ± 0.05	4.53 ± 0.17	2.00 ± 0.10	0.33	0.21	0.50	0.71	< 0.01	<< 0.01	0.01	0.11	0.03	0.36
SGL*	1003	267	7.5	0.75 ± 0.02	4.50 ± 0.07	2.00 ± 0.28	1.59	0.96	2.44	1.14	0.01	<< 0.01	0.02	0.53	0.33	0.85
WQU*	3711	356	7.7	0.85 ± 0.02	5.31 ± 0.10	2.00 ± 0.03	1.60	0.92	2.56	1.08	0.09	0.05	0.19	0.79	0.43	1.44

* indicates the seismic source zones in eastern Canada. N: Total number of earthquakes. T: Catalog length in years. Mx is the maximum expected earthquake moment magnitude based on the 2015 Canadian Seismic Hazard Map. a and b values are earthquake parameters estimated from linear regression. Med, Min, and Max refer to the median, minimum, and maximum estimates. $\dot{M}_0^G$ denotes the geodetic moment rate estimate while $\dot{M}_0^{SK}$ and $\dot{M}_0^{SG}$ denote the seismic moment rate from moment summation and truncated Gutenberg-Richter distribution.

Similarly, the magnitude of completeness indicating the minimum earthquake magnitude that can be completely detected varies from 1.50 to 2.57. The maximum shear strain rate within the seismic source zone is a few nanostrain per year (0.71×10^{-19} - 5.11×10^{-19}). However, it appears that the maximum shear strain is higher (~2-3 times) in seismic source zones in western Canada (> 1.3×10^{-19} yr^{-1}) than eastern Canada (< 1.2×10^{-19} yr^{-1}) (see Table 1). Since the geodetic moment rate is related to the area, we normalize the estimates with the defined source area to compare the estimate across the zones (Figure 1a). The estimated rate of strain accumulation is the highest ($\dot{M}_0^G$ > 10^{12} Nm/km²/yr) within the MVI, OLY, PUG, and SVI seismic source regions along the CSZ (see Figure 4). An intermediate rate of strain accumulation (1.0×10^{11} - 4.1×10^{11} Nm/km²/yr) is found in the BCS, BCN, FORS, FORN, NVI, WASH, BSL, CHV, SGL, and WQU. Enhanced strain accumulation has been reported by Tarayoun et al. (2018) within the CHV seismic source zone. However, the ALB, LSP, NAP, and NON seismic source zones are characterized by geodetic moment rates lower than 10^{11} Nm/km²/yr (Table 1 and Figure 4). The rates of seismic moment released by earthquakes are the highest (>5×10^{17} Nm/yr) within the seismic source zones along the Pacific coast in western Canada (i.e. MVI, SVI, NVI, OLY, and PUG) and LSP in eastern Canada (see Table 1 and Figure 4).

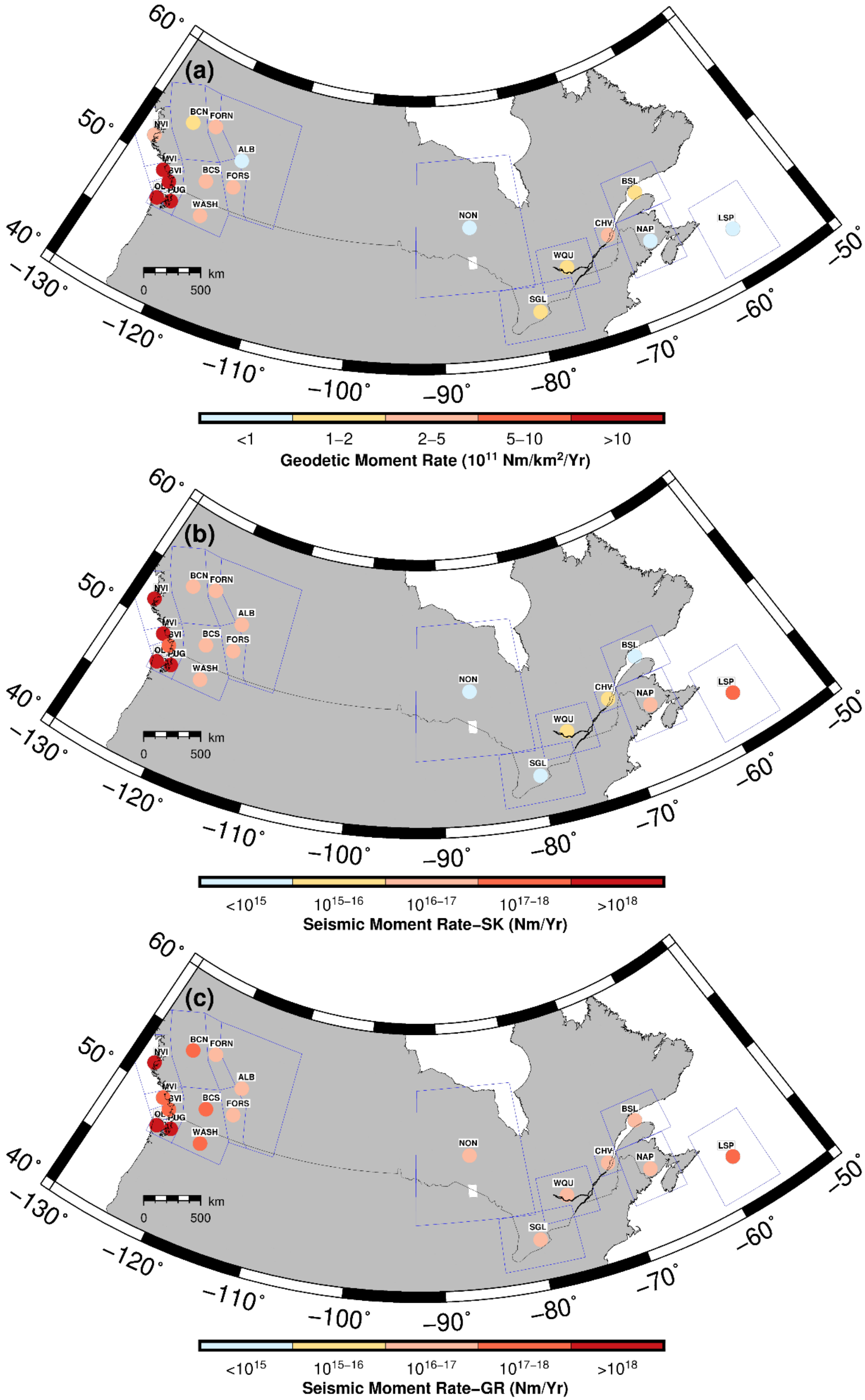

(a)
BCN
FORN
NVI
ALB
MVI
SVI
BCS
FORS
OL
PUG
WASH
NON
BSL
LSP
CHV
NAP
WQU
SGL
km
0
500
60°
50°
40°
−130°
−120°
−110°
−100°
−90°
−80°
−70°
−60°
−50°
<1
1–2
2–5
5–10
>10
Geodetic Moment Rate (10^{11} Nm/km^2/Yr)
(b)
<10^{15}
10^{15-16}
10^{16-17}
10^{17-18}
>10^{18}
Seismic Moment Rate–SK (Nm/Yr)
(c)
<10^{15}
10^{15-16}
10^{16-17}
10^{17-18}
>10^{18}
Seismic Moment Rate–GR (Nm/Yr)

Figure 4. Estimates of the moment rates within each seismic source zones from (a) geodetic data (b) earthquake data using the cumulated Kostrov summation method (c) earthquake data using the truncated Gutenberg-Richter distribution method. The upper and lower bound of the estimates are presented in Table 1. The locations of existing seismic source zones and the main tectonic features in the study area are shown on the maps and defined in Figure 1a. The black line defines the Canada-US border to the south.

Most of the other seismic source zones (i.e. ALB, BCN, BCS, FORN, FORS, WASH, CHV, NAP, and WQU) are characterized by intermediate seismic moment release (between 10^{16} and 10^{18} Nm/yr). However, an anomalously low rate of seismic moment release (≤10^{16} Nm/yr) is observed in BSL, NON, and SGL seismic source zones (see Table 1). Due to better data constraints, we obtained reliable results in seismic source zones (e.g., BCN, MVI, FORN) where Mazzotti et al. (2011) reported their inability to obtain a satisfactory result due to poor catalog statistics and GNSS data coverage. For more local results useful for seismic hazard modelers, we present estimates of earthquake parameters, geodetic and seismic moment rate at 45 actual seismic source zones used in the national seismic hazard model (Halchuk et al. 2015) in Table S4 and Figure S5. The estimated moment rates are similar to the abovementioned values in eastern and western Canada.

5 Discussion

5.1 Seismic versus Geodetic Moment Rate Across the Study Area

Here, we quantify the percentage of the accumulated strain that has been released seismically by comparing the rate of seismic moment release ($\dot{M}_0^{SG}$ and $\dot{M}_0^{SK}$) to the rate of strain accumulation ($\dot{M}_0^{G}$) at each grid (Figure 5). The pattern of moment rate ratio computed using the two seismic moment rate estimates are similar, but we observe a general reduction of the moment rate ratios for the Kostrov summation ($\dot{M}_0^{SK}$) method (see Figures 5a and 5b). As suggested by previous studies, the seismic moment rate estimated from the Kostrov summation ($\dot{M}_0^{SK}$) method may be underestimated due to incompleteness in the earthquake catalog (i.e. the lack of large magnitude earthquakes and missing small magnitude events). The magnitude of completeness (M_c) estimated at each 2° x 2° grids range in the interval 1.50 – 2.57 suggesting that our catalog is missing small magnitude earthquakes probably due to non-uniform seismic station density across the study area. Therefore, the estimated $\dot{M}_0^{SK}$ may not adequately capture the long-term pattern of seismicity unlike the estimates from the truncated Gutenberg–Richter distribution method (e.g., Mazzotti et al., 2011; Palano et al., 2018).

For most of the study area, the rate of geodetic strain accumulation is larger than the rate of seismic moment release by at least ~1-2 orders of magnitude (see Figure 5a). Therefore, the computed ratios are generally small (< 20%), indicating an apparent imbalance between the two moment rate estimates and suggesting that only a small fraction of the geodetically measured strain has been released seismically (e.g., Kao et al., 2018). The lack of earthquakes or an insufficient number of events in some parts of the study region is reflected by several void grids indicating our inability to constrain the earthquake a and b values for $\dot{M}_0^{SG}$ computation (see Figure 5b). The widespread observation of strain accumulation in the crust without corresponding release by earthquakes in Canada can be partly attributed to aseismic deformation by the well-known process of GIA that is prevalent across the continent (Kreemer et al., 2018;

Kuchar et al., 2019; Mazzotti et al., 2011; Peltier et al., 2016, 2018; Pursell et al., 2018; Simon et al., 2016). Alternatively, the strain can continuously accumulate in the crust in the absence of aseismic deformation, and given the right conditions, can potentially be released as earthquakes in the future. Additionally, the lack of agreement between the seismic and geodetic moment rate may also be related in part to inaccuracies and limitations in the dataset and the methodology as revealed by previous studies (e.g., Mazzotti et al., 2011; Palano et al., 2018). These potential causes are further discussed in subsequent sections 5.2 and 5.3.

We found that most grid points with moment rate ratios >1% are associated with previously identified seismic source zones in western and eastern Canada (Figure 5). Specifically, the $\frac{\dot{M}_0^{SG}}{\dot{M}_0^{G}}$ and $\frac{\dot{M}_0^{SK}}{\dot{M}_0^{G}}$ ratios are < 10% for ALB, BCN, BCS, FORN, FORS, BSL, NAP, NON, and SGL. It ranges between 10% and 50% for source zones MVI, SVI, WASH, CHV, LSP, and WQU, suggesting that a significant proportion of the accumulated strain has been released by earthquakes. In seismic source zones NVI, OLY and PUG, we observe a high percentage of strain release that can approach or exceed 100%, suggesting the possibility of a complete seismic release of accumulated strain (Figure 5).

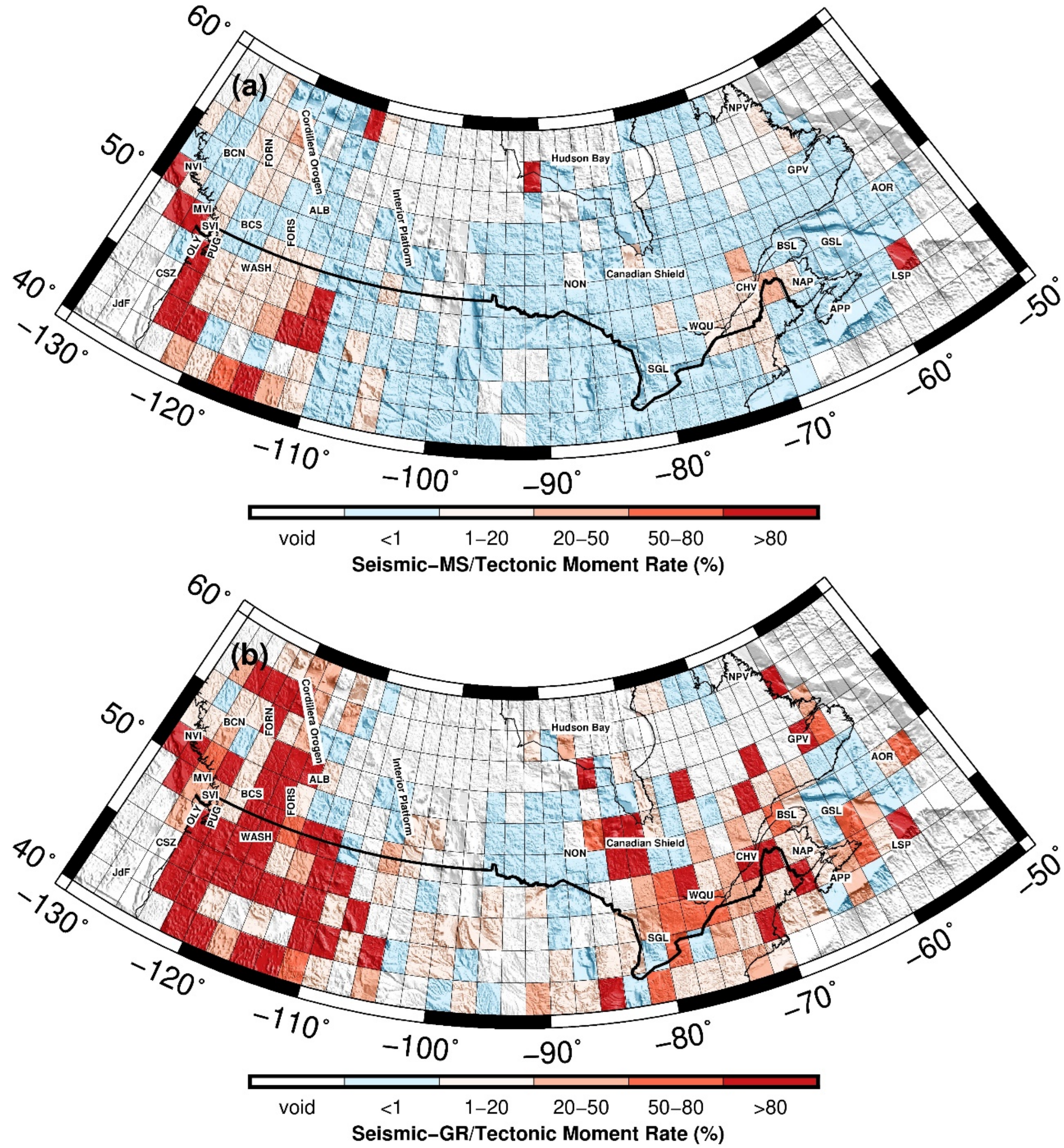

Figure 5. The ratio of seismic and geodetic moment rate (a) using seismic moment rate estimated from the cumulated Kostrov summation method (b) using seismic moment rate estimated from the truncated Gutenberg-Richter distribution method. The upper and lower bound estimates are presented in Table S3. The location of existing seismic source zones and the main tectonic features are indicated on the maps and defined in Figure 1. The thick black line defines the Canada-US border to the south.

The areas of the intermediate-to-high percentage of moment rate ratios coincide with locations of active tectonics, suggesting that the observation can be directly linked to ongoing tectonic processes in these regions. For example, along the Pacific Coast and Vancouver Island, the ongoing subduction of the oceanic Juan de Fuca and Explorer plates beneath the NA causes enhanced seismicity in the region. Likewise, along the St. Lawrence River Valley in eastern Canada, possible reactivation of crustal faults by regional stress fields has been reported to be the primary driver of increased seismicity and deformation in the region

(Tarayoun et al., 2018). A similar observation was made by D'Agostino et al. (2014) in the tectonically complex region of Apennines, Italy to rule out significant aseismic deformation in the region and this may also be the case in Canada. The observation of high percentage moment rate ratios may also imply that the seismic moment released by earthquakes over the study period occurred at a rate much closer to the rate of strain accumulation. Such a good agreement between the seismic and geodetic moment rates may suggest that the current and the future rate of seismicity in these seismic source zones may be very similar, thereby providing us a window looking into future earthquake scenarios at these locations (e.g., Gonzalez-Ortega et al., 2018; Hyndman et al., 2003; Mazzotti et al., 2011; Pancha et al., 2006).

5.2 Aseismic Strain Release by GIA-induced Deformation

The widespread low percentage ratio between the seismic and the geodetic moment rate in many source zones implies that only a small proportion of the accumulated strain is eventually released by earthquakes. Hence, we considered other potential means of strain accumulation and release processes without elevated seismicity such as GIA. However, more recent studies have revealed that besides GIA, structural inheritance contributes significantly to the observed elevated rate of strain accumulation, especially at locations of known crustal weakness such as the St. Lawrence Valley in eastern Canada (e.g., Tarayoun et al., 2018). Besides, factors related to catalog incompleteness and limited spatial resolution of GNSS observations have also been identified to contribute to the observed discrepancies (Palano et al., 2018). This raises the question of how much of the observed deformation can be fairly attributed to the ongoing GIA processes. As noted by Mazzotti et al. (2011), this is an important scientific question to answer to integrate GNSS strain rates into regional probabilistic seismic hazard analysis. Therefore, we move a step further to quantify the percentage of the observed discrepancy between the seismic and geodetic moment rates that can be explained by predictions from one of the existing GIA models while acknowledging its limit of accuracy ($\delta_{GIA} = \frac{\dot{M}_0^{GIA}}{(|\dot{M}_0^{G} - \dot{M}_0^{S}|)} \times 100$). For this purpose, we made use of the recently published ICE-6G-D(VM5a) global GIA model which was developed from an extensively validated ice history dataset in conjunction with a 1-D earth model (VM5a) characterized by laterally homogeneous layered Earth structure and calibrated by paleo-sealevel data and GNSS observations (Peltier et al., 2015; 2018).

As a first step, we estimate the strain rate and moment rate based on the horizontal velocities predicted by the GIA model (mostly ~2 mm/yr or less) as shown in Figure 6. The maximum and minimum principal component of the strain rate tensors ranges from -0.9 to 5 nstrain/yr and -1.4 to 1.2 nstrain/yr, respectively, and the maximum shear strain rates range from 0 to 2.88 nstrain/yr (see Figure 6a). The principal axes of the strain rates are characterized mostly by extensional strain throughout Canada, however, localized contractional strain rates can be observed in the Appalachian region in eastern Canada (Snay et al., 2016; see Figure 6b). The computed GIA moment rate ($\dot{M}_0^{GIA}$) ranges between 1.5×10^{15} and 1.7×10^{17} Nm/yr and shows a simple pattern of variation within the Canadian landmass (Figure 6c). The $\dot{M}_0^{GIA}$ values are generally <2×10^{16} Nm/yr around the western, northern, and eastern edges but mostly fall in the range of 2–4 × 10^{16} Nm/yr within the study area (Figure 6c). In comparison to the geodetic moment rate (Figure 6d and Table S3), the GIA moment rate estimates are ~1–4 times smaller in the study area except for the Canadian Cordillera where it could be as much as 10 times smaller (e.g., King et al., 2010). This suggests, to first order, that the measured GNSS strain cannot be explained by the ICE-6G-D(VM5a) GIA model across Canada. However, few locations exist (e.g., within Hudson Bay, Interior Platform, and Canadian Shield) where the magnitude of the GIA and GNSS moment rate are comparable (with a ratio between 0.8 and 1.2), suggesting a low probability of strain release by damaging earthquakes (Figure 6d).

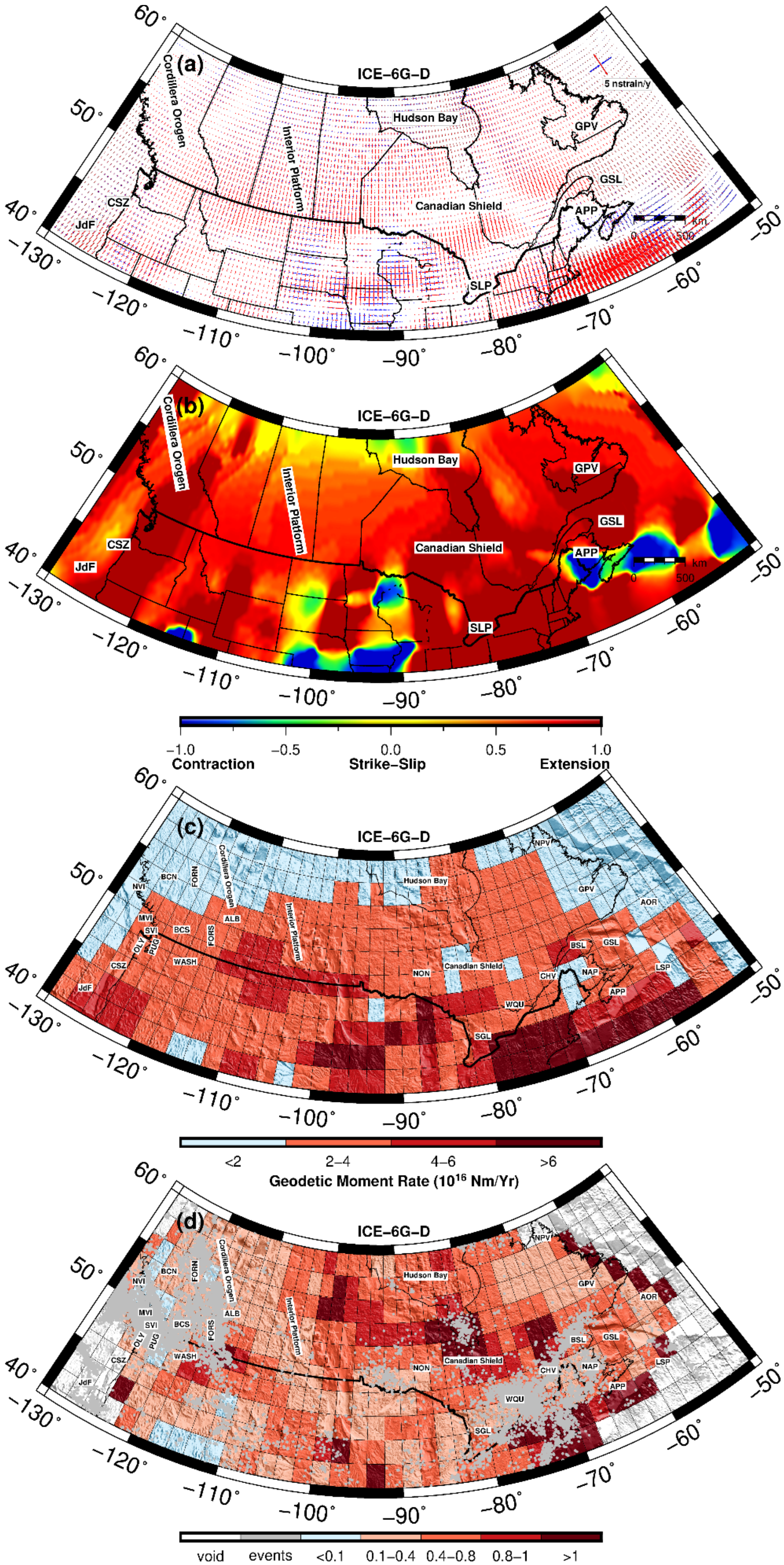

(a)
ICE-6G-D
5 nstrain/y
Cordillera Orogen
Interior Platform
Hudson Bay
Canadian Shield
GPV
GSL
APP
SLP
CSZ
JdF
km
0
500
(b)
ICE-6G-D
Cordillera Orogen
Interior Platform
Hudson Bay
Canadian Shield
GPV
GSL
APP
SLP
CSZ
JdF
−1.0
−0.5
0.0
0.5
1.0
Contraction
Strike-Slip
Extension
(c)
ICE-6G-D
NPV
BCN
FORN
NVI
MVI
SVI
OLY
PUG
BCS
FORS
ALB
WASH
CSZ
JdF
Cordillera Orogen
Interior Platform
Hudson Bay
GPV
AOR
BSL
GSL
Canadian Shield
NON
CHV
NAP
LSP
APP
WQU
SGL
<2
2–4
4–6
>6
Geodetic Moment Rate (10^{16} Nm/Yr)
(d)
ICE-6G-D
NPV
BCN
FORN
NVI
MVI
SVI
OLY
PUG
BCS
FORS
ALB
WASH
CSZ
JdF
Cordillera Orogen
Interior Platform
Hudson Bay
GPV
AOR
BSL
GSL
Canadian Shield
NON
CHV
NAP
LSP
APP
WQU
SGL
void
events
<0.1
0.1–0.4
0.4–0.8
0.8–1
>1
60°
50°
40°
−130°
−120°
−110°
−100°
−90°
−80°
−70°
−60°
−50°

Figure 6. Estimates based on the ICE6G GIA model. (a) Strain rate field based on the predicted horizontal velocities from ICE-6G-D at grid spacing 0.5° x 0.5° across the study area. The red and blue crosses indicate the orientation and magnitude of the extensional and contractional strain rate respectively. (b) The style of the strain rate tensor is defined by Kreemer et al. (2014). The scale ranges from -1 to +1 corresponding to when both principal axes are compressional and extensional respectively. (c) Estimates of the GIA moment rates at a 2° x 2° grid across the study area. The upper and lower bound estimates are presented in Table S3. (d) The ratio of the GIA and geodetic moment rate overlay by the earthquake epicenters. The thick black line defines the Canada-US border to the south and the main geological and tectonic features and abbreviations are defined in Figure 1.

At these locations, the observed strain rate is the result of aseismic deformation by GIA, thus no tectonic strain is accumulated. However, previous studies have indicated the possibility of stress changes due to GIA to combine with background tectonic stress on existing fault zones to trigger earthquakes (Steffen et al., 2014; Brandes et al., 2015). Therefore, we infer that locations with comparable GIA to GNSS moment rates and low background tectonic stress (e.g., west of Hudson Bay; see Figure 6d) are recommended sites in Canada for the development of critical facilities to reduce their exposure to damaging earthquakes.

Subsequently, we hypothesize that the total accumulated strain should be equal to the summation of the strain released seismically by earthquakes and those released aseismically by the ongoing process of GIA in the study area. This allows us to quantify supposed GIA-induced deformation which we expressed as a fraction of the absolute difference between the geodetic and seismic moment rate as shown in Figure 6. The result obtained using the seismic moment rate from the $\dot{M}_0^{SK}$ and the $\dot{M}_0^{SG}$ method generally follows a similar pattern for non-void grids (Figures 7a and 7b). The estimated percentage of moment rate discrepancy that can be accounted for by GIA-induced deformation (δ_{GIA}) is generally >40% in eastern Canada but mostly <20% in western Canada except for southeastern Alberta (ALB) (Figure 7). Specifically, in the area south of Hudson Bay (e.g., Canadian Shield) predictions from the GIA model can account for most (>80%) of the observed discrepancies (e.g., Tarayoun et al., 2018). Similarly, in eastern Canada, a band through the seismic source zones along the St. Lawrence Valley (e.g., SGL, WQU, CHV, and NAP) and along the Canada-USA border is characterized by a relatively lower δ_{GIA} percentage (between 20% and 60%, Figure 7). Tarayoun et al. (2018) found that within the St. Lawrence Valley, strain rates are on average 2–11 times higher than the surrounding regions and 6–28 times higher than the GIA-predicted strain rates. They attributed their observation of strong strain amplification to inherited tectonic structure and associated lithospheric rheology weakening within the St. Lawrence Valley. Therefore, our observation of reduced δ_{GIA} in this region could provide further evidence for enhanced strain accumulation due to inherited tectonic structures (e.g., reactivation of Iapetus structures) as reported by Tarayoun et al. (2018) within these seismic source zones.

We observe a decreasing percentage of δ_{GIA} as we move from eastern Alberta (20–40%) westward to the Cordillera and the Pacific Coast (Figure 7). The lithosphere beneath the Cordillera has sustained major deformation due to strain transferred inland from the CSZ as revealed by several studies (e.g., Audet et al., 2019; Chen et al., 2019; Estève et al., 2020; McLellan et al., 2018). Several studies have also revealed that the Cordillera is underlain by hotter and buoyant mantle material which differs significantly from eastern Canada (Bao et al., 2016; Peltier et al., 2015, 2018; Wu et al., 2019). Therefore, the nature of the mantle rheology within the Cordillera and the Pacific Coast may have allowed for a fast response of the lithosphere to PGR thereby limiting the present-day effect of GIA in western Canada (James et al., 2001). Global GIA models generally use a layered Earth model with the assumed upper mantle viscosity much higher than what we expect beneath the Canadian Cordillera (e.g., James et al., 2001). As a result, the ICE-6G-D model provides an upper limit of the present-day Earth's viscous responses to the Laurentide and Cordillera Ice Sheet in western Canada. The regional GIA model (James et al., 2001) uses more realistic viscosity values and predicts a much smaller (~ 0.1 mm/yr) surface deformation rate due to the Cordillera Ice Sheet. Despite this, we conclude that GIA from the past ice melting cannot fully explain the discrepancy we see in western Canada. The remaining difference is likely contributed from a combination of different tectonic and non-tectonic related deformation sources. Deformation induced by ice melting since the little ice age (LIA) is prevalent in the Canadian Cordillera (Larsen et al., 2006) and Alaska. The LIA related GIA deformation can produce a present-day deformation rate on the order of a few mm/yr across western Canada, comparable to our observed strain rate estimates. However, deformation related to LIA GIA is likely limited to the coastal mountain region and has limited spatial distribution. We suspect that deformations related to plate boundary subduction (Li et al., 2018) and upper plate crustal faults (Elliott et al., 2010; McCaffrey et al., 2013) may have contributed significantly to the observed strain rate. To fully understand the deformation mechanisms in western Canada, an improved GIA model that accounts for 3-D lateral variation in mantle rheology, including the effect due to the LIA melting history, is needed. Deployment of a dense GNSS network over a sufficiently long period will also be required to confidently identify and distinguish deformation sources from crustal faults and plate subduction.

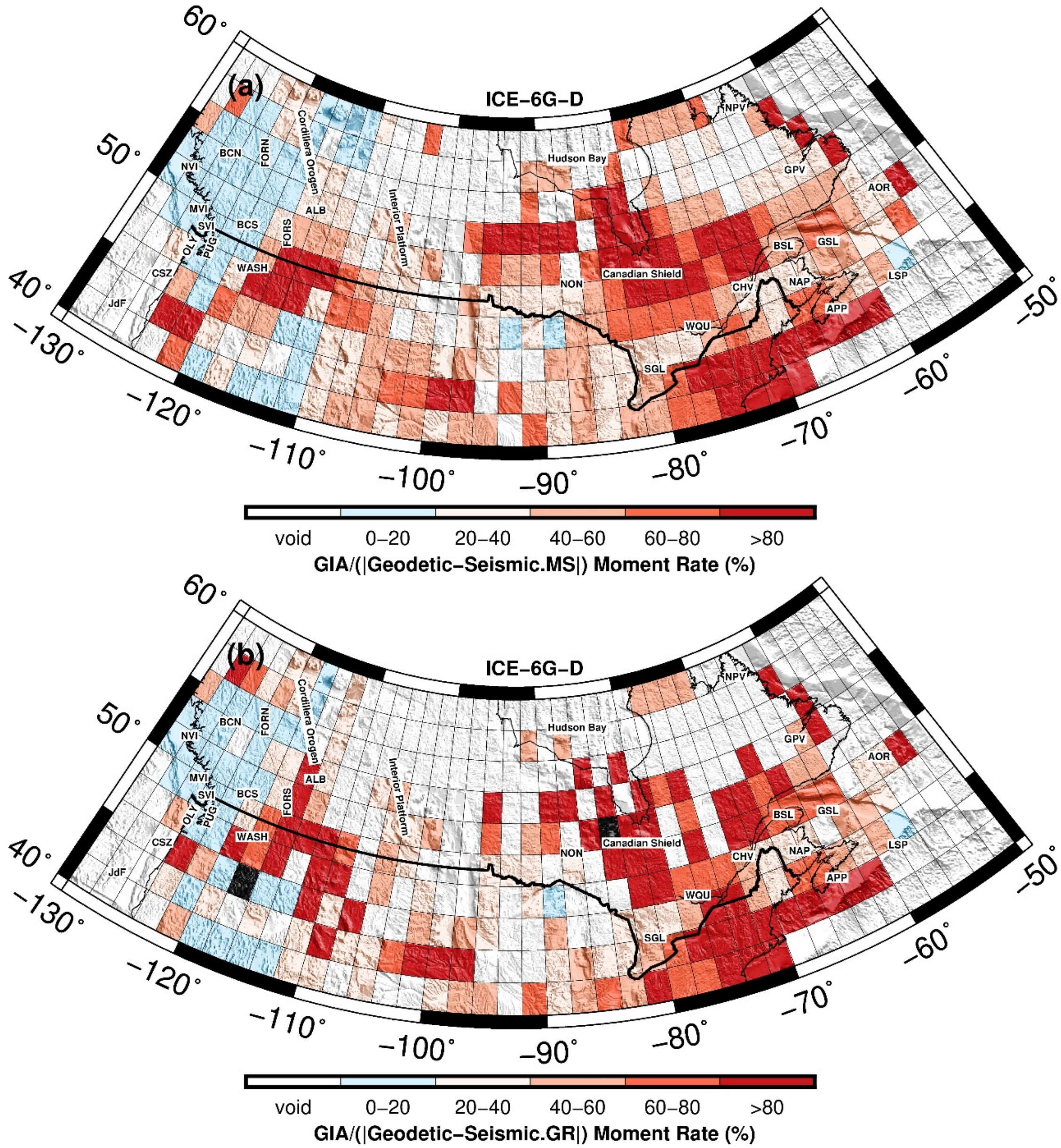

Figure 7. The percentage ratio of the GIA moment rate and the absolute difference between the geodetic and seismic moment rate estimated from (a) the cumulated Kostrov summation method (b) the truncated Gutenberg-Richter distribution method. The locations of existing seismic source zones and the main tectonic features are indicated on the maps as defined in Figure 1. The thick black line defines the Canada-US border to the south.

5.3 Potential Earthquake Hazards

It is well accepted that the probability of earthquake occurrence largely depends on the absolute strain level (D'Agostino, 2014). Consequently, several studies have used estimates of seismic and geodetic moment rates, moment deficits, and earthquake recurrence times of an assumed earthquake magnitude to assess the potential seismic hazard in different regions (e.g., Jenny et al., 2004; Kreemer et al., 2000;

Mazzotti et al., 2011; Middleton et al., 2018; Pancha et al., 2006). We estimate the available moment budget in the crust by taking the difference between the total amount of seismic moment released by earthquakes and the accumulated moment derived from geodetic measurement over the catalog duration $\left(\left(\dot{M}_0^G - \dot{M}_0^S\right) \times T\right)$. The moment budget is negative (i.e. moment excess) when the total amount of moment release exceeds that of tectonic strain accumulation and vice versa (i.e. moment deficit). For the moment budget computation, we used the seismic moment rate estimated from the truncated GR relation since it is generally accepted to be less affected by catalog incompleteness and more representative of the long-term seismicity (e.g., Deprez et al., 2013; Hyndman & Weichert, 1983; Kreemer et al., 2002; Mazzotti et al., 2011; Ward, 1998a, 1998b). Subsequently, we compute the equivalent earthquake magnitude based on the moment-magnitude formulation ($M_w = \frac{2}{3} log M_0 - 9.05$) of Hanks and Kanamori (1979). Based on the conservation of the total moment, we estimate the frequency of the equivalent-magnitude earthquakes $\left(T(M) = \frac{\beta M_{max}^{1-\beta} M^{\beta}}{\dot{M}_0(1-\beta)}\right)$ assuming that seismicity follows the empirical Gutenberg–Richter (GR) law (e.g., Middleton et al., 2018). These estimates are presented in Table 2 for individual seismic source zones in western and eastern Canada. We observe that the seismic moment rate ($\dot{M}_0^{SG}$) and geodetic moment rate ($\dot{M}_0^G$) have good agreement (with a ratio between 0.9 and 1.3) within the PUG, OLY, and NVI seismic source zones. The next level of agreement between the seismic and geodetic moment rates (with a ratio of ~0.5) is found within the LSP and MVI seismic source zones. Near unity, ratios indicate that a large proportion of the accumulated strain has been released by earthquakes in these seismic source zones and thus having a low potential of having major damaging earthquakes in the near future (e.g., Deprez et al., 2013; D'Agostino, 2014; Gonzalez-Ortega et al., 2018; Palano et al., 2018). This observation confirms the result of Mazzotti et al. (2011) who found good agreement between the two moment rates in PUG (0.77) and MVI (0.83) (Table 2; Hyndman et al., 2003).

Within the PUG and OLY seismic source zones, we observe moment excesses (≤-0.4 x 10^{20} Nm) resulting from a relatively large seismic moment rate. This can be attributed to the occurrence of large magnitude earthquakes in a small area or indicate that the strain released by earthquakes in this seismic source zone was accumulated over periods longer than the catalog duration (e.g., Rontogianni, 2010). In all other seismic source zones, the ratio of seismic to geodetic moment rates is <1, indicating a moment deficit in the range of 1.4 x 10^{19} – 4 x 10^{20} Nm to be released by overdue earthquakes (e.g., Palano et al., 2018). Based on the moment-magnitude formulation (Hanks & Kanamori, 1979), the strain accumulated in the crust is equivalent to a single earthquake with Mw ranging from 6.7 to 7.7 (Table 2). Instead of the occurrence of a single large magnitude earthquake, the strain may also be released incrementally by several smaller events (Clarke et al., 1997). Either way, the scenario represents an elevated seismic risk in these source zones. However, this may not be the case for seismic source zones located in eastern Canada where there is a high likelihood of aseismic release of accumulated strain as previously discussed (Figure 7). The computed earthquake recurrence times based on the geodetic moment rate, earthquake b-value, and assumed maximum magnitude for $M_w \geq 6$ and $M_w \geq 7$ fall in the ranges of ~6–178 and 77–5439 years, respectively, across various seismic source zones (Middleton et al., 2018; see Table 2). This estimate provides a measure of the rate of occurrence of large magnitude earthquakes needed to seismically balance the accumulated strain. The earthquake recurrence times for magnitude $M_w \geq 6$ and $M_w \geq 7$

earthquakes are relatively shorter (e.g., <15 years and <200 years, respectively) for seismic source zones located along the active Pacific Coast (e.g., NVI, SVI, MVI, OLY, PUG) in western Canada while it is about 2–9 times longer for seismic source zones in eastern Canada (e.g., BS, LSP, CHV) (see Table 2).

Table 2: Estimates of moment rate ratios, moment budget, and earthquake recurrence times

Seismic Source zones	$\dot{M}_0^{SK}/\dot{M}_0^{SG}$		$\dot{M}_0^{SG}/\dot{M}_0^{G}$		Moment Budget (10^{20} Nm)	Equivalent Magnitude (Mw)	Estimates based on $\dot{M}_0^{G}$					
							Recurrence Time-Yrs (M >= 6)			Recurrence Time-Yrs (M >= 7)		
	This Study	Mazzotti et al. (2011)	This Study	Mazzotti et al. (2011)			Estimate	Lower	Upper	Estimate	Lower	Upper
ALB	0.23	0.85	0.03	6.4×10^{-3}	3.87	7.7	64	41	106	1946	1261	3233
BCN	0.28	5.93	0.05	3.3×10^{-5}	2.12	7.5	6	4	10	132	91	203
BCS	0.14	0.04	0.14	5.2×10^{-2}	1.26	7.4	10	7	15	141	98	215
FORN	0.50	0.11	0.07	0.21	0.82	7.2	19	13	29	433	296	674
FORS	0.36	0.56	0.09	0.34	0.59	7.2	178	123	274	5439	3744	8375
MVI	3.04	2.28	0.49	0.83	0.99	7.3	8	6	12	104	72	159
NVI	1.53	0.10	0.91	0.13	0.14	6.7	6	4	10	77	53	120
OLY	1.44	0.12	1.27	5.6×10^{-2}	-0.40	-7.0	14	10	22	113	77	175
PUG	0.63	0.33	1.33	0.77	-0.66	-7.2	13	9	19	93	64	143
SVI	2.06	0.31	0.30	0.12	1.22	7.4	11	8	17	135	93	206
WASH	0.06	0.16	0.27	0.10	0.94	7.3	13	9	21	212	144	332
BSL*	0.01		0.03		1.35	7.4	57	39	91	1426	958	2259
CHV*	0.33		0.19		0.63	7.2	97	61	167	1481	935	2552
LSP*	3.55		0.47		0.23	6.9	53	34	88	654	420	1100
NAP*	0.37		0.06		1.46	7.4	23	15	39	362	230	616
NON*	0.03		3.8×10^{-3}		3.60	7.7	9	6	14	224	151	355
SGL*	0.01		0.05		2.87	7.6	11	7	18	144	94	238
WQU*	0.12		0.16		1.52	7.4	30	19	52	566	353	989

* indicates seismic source zones in eastern Canada. $\dot{M}_0^{G}$ denotes the geodetic moment rate estimate while $\dot{M}_0^{SK}$ and $\dot{M}_0^{SG}$ denote the seismic moment rate from moment summation and truncated Gutenberg-Richter distribution. The upper and lower bound of the recurrence times are obtained by propagating the b-value uncertainty and using the corresponding upper and lower bound estimates in Table 1.

Generally, the estimate of the moment release rate is regarded as highly reliable only when the earthquake catalog spans several recurrence times of large earthquakes (Jenny et al., 2004). In our case, the catalog length is 2 – 75 times longer than the estimated recurrence time for M_w ≥6 across various seismic source zones. For M_w ≥7, the catalog length is only ~1 – 6 times longer than the estimated recurrence time in some seismic source zone (e.g., BCN, BCS, FORN, MVI, NVI, OLY, PUG, SVI, WASH, NAP, SGL, and NON) whereas the catalog duration is ~1 – 11 times shorter than the estimated recurrence time in others (e.g., ALB, FORS, BSL, CHV, LSP, and WUQ) (see Table 2). Previous studies have found estimates of earthquake recurrence times to be subject to very high uncertainties and largely dependent on how the accumulated strain is been reset by the occurrence of large magnitude earthquakes in the region (D'Agostino, 2014; Weldon et al., 2004). Likewise, the elastic strain can be cumulatively stored in the crust without been released for a period longer than that predicted by the recurrence interval, thus leading to an overdue (and often larger) earthquake. Additional limited knowledge on the strain level before the GNSS deployment further contributes to these uncertainties (D'Agostino, 2014; Field et al., 1999; Mazzotti et al., 2011). Therefore, we suggest that our estimates of earthquake recurrence intervals and inferences based on them should be taken conservatively.

5.4 Comparison of Seismicity with Crustal Deformation Rates

On a global scale, a strong correlation between the geodetic moment rates and the frequency of earthquakes has been observed at different tectonic settings (e.g., Bird et al., 2010; Kagan, 1999; Kreemer et al., 2002). However, there are regions where this relationship has been reported to be invalid (e.g., Masson et al., 2004). In Figure 8, we show the relationship between geodetic moment rates and the number and magnitudes of earthquakes in Canada.

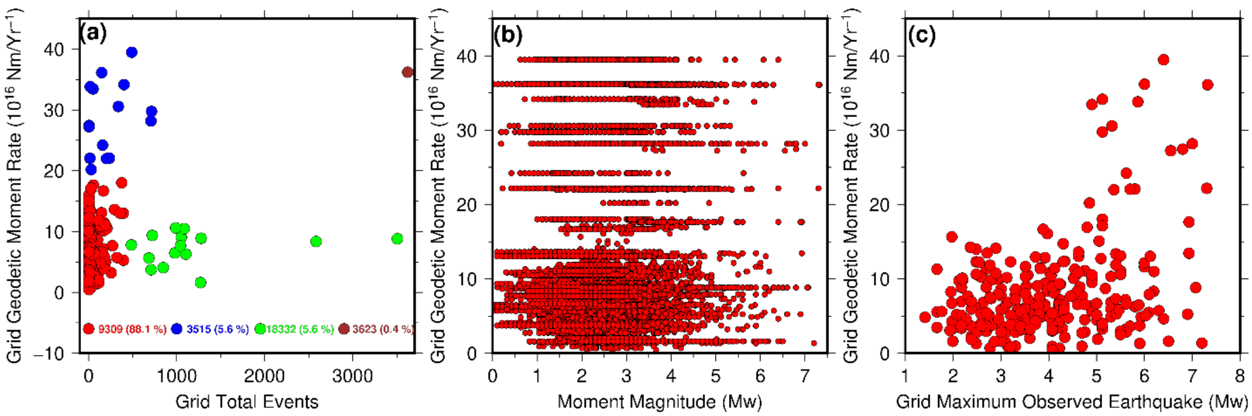

Figure 8. Comparison between the geodetic moment rate and seismicity in the study area (a) geodetic moment rate and earthquake count in each grid (b) spatial correlation of the geodetic moment rate and the earthquake magnitudes (c) geodetic moment rate and the maximum observed earthquake magnitude in each grid. We note that each dot in (b) corresponds to one earthquake while each dot in (a) and (c) correspond to a 2° x 2° grid.

Most of the grid points (88.5%) fall into the category of a relatively low geodetic moment rate (< 1.8 x 10^{17} Nm/yr) and a small total number of earthquakes (< 400, red circles in Figure 8a). This category accounts for ~20.5% of the total number of earthquakes in our catalog. On the opposite, there are regions (e.g., within NVI, OLY, and PUG) characterized by relatively low numbers of earthquakes and high geodetic moment rates (up to ~4.0 x 10^{17} Nm/yr; blue circles in Figure 8a). They account for ~7.7% of the total number of earthquakes in the catalog and 5.2% of the total grid points. The third category is characterized by an intermediate-to-low geodetic moment rate (< 1.5 x 10^{17} Nm/yr) with many earthquakes (e.g., within WQU, CHV, FORN, and FORS). Regions in this category account for the largest proportion of earthquakes in the catalog (~43.4%) but only 5.9% of the grid points (lime circles in Figure 8a). The last category represents grid points characterized by high geodetic moment rates (> 3.0 x 10^{17} Nm/yr) and many earthquakes (>2500) (e.g., within SVI). Only one of the 400 grid points (0.4%) is in this category, but it accounts for ~8% of the total number of earthquakes in our catalog (the brown circle in Figure 8a). The first and last categories agree with the linear correlation between the seismicity and the strain rates reported in the literature (e.g., Kagan, 1999; Kreemer et al., 2002). However, the second and third categories appear anomalous because the seismicity recorded in those regions is significantly lower or higher than expected, suggesting that the globally observed correlation may not hold for at least some part of Canada. High seismicity in low strain regions may indicate that other factors (e.g., structural inheritance) besides strain accumulation may be responsible for earthquake generation in the region (e.g., Tarayoun et al., 2018) whereas low seismicity in high strain regions may point to ongoing aseismic deformation or overdue earthquakes (e.g., Gonzalez-Ortega et al., 2018; Middleton et al., 2018; Palano et al., 2018).

Although small magnitude earthquakes (M≤4) appear to cluster at regions of relatively low geodetic moment rates (< 1.5 x 10^{17} Nm/yr), it is apparent that earthquakes of all magnitudes can occur in regions with either high or low geodetic moment rates (Figure 8b). This may indicate a significant spatial variation for the seismogenesis of large earthquakes (Riguzzi et al., 2012). Since large magnitude earthquakes are of primary importance to seismic hazard, we compare the magnitude of the largest earthquake observed in each cell with the corresponding geodetic moment rate and the results are plotted in Figure 8c. The magnitude of the largest earthquake observed in each cell spread across a wide range of values (M_w 1.4–7.3) for regions associated with intermediate-to-low geodetic moment rates (<1.5 x 10^{17} Nm/yr). However, not a single cell with a high geodetic moment rate (>1.5 x 10^{17} Nm/yr) can be associated with a maximum earthquake magnitude less than M_w 5 (Figure 8c). The strong correlation between epicenters of large earthquakes and areas with high geodetic moment rates suggests that there is a higher probability of seismic risk at locations characterized by high geodetic moment rates (e.g., along the Canada-USA border in central Canada; see Figure 3a). This observation agrees with the reported of Zeng et al. (2018) in California and Nevada, USA but contradicts the observation of Riguzzi et al. (2012) in Italy.

Conclusions

Taking advantage of the recent improvements in seismic and geodetic station coverage across Canada, we exploit the principle of moment conservation to obtain an improved picture of the interplay between the geodetically measured strain accumulation and the moment released by earthquakes. To achieve this, we performed a detailed analysis of data from all available GNSS stations and compiled the most complete earthquake database spanning over 486 years. This led to robust estimates of the scalar seismic and geodetic moment rates on a regular 2° × 2° grid across the study area. A higher rate of strain buildup than seismic moment released by earthquakes is observed in most of the study areas and we attribute it to long-term regional aseismic deformation related to the ongoing process of PGR, especially in eastern Canada. At locations with limited evidence for aseismic deformation (e.g., existing seismic source zones), we speculate that the unreleased strain is been stored cumulatively in the crust and may be released as earthquakes in the future. Therefore, the occurrence of individual, large-magnitude events with long-term average recurrence intervals is required to explain the pattern of moment release and seismically deplete the accumulated strain. Within the limit of GIA uncertainties, we recommend that areas of zero-to-low background seismicity with geodetic and GIA moment rates close to unity are the potential safe site for installation of critical facilities that are highly vulnerable to earthquake hazards. Our attempt to quantify the GIA-induced deformation has the potential to motivates future research on the integration of GNSS strain rates in seismic hazard studies for a more complete assessment in Canada.

Acknowledgments

Predictions of the current GIA uplift from the ICE-6G_D (VM5a) model were downloaded from http://www.atmosp.physics.utoronto.ca/~peltier/data.php. The GNSS station information and computed horizontal velocities are downloaded from the Nevada Geodetic Laboratory http://geodesy.unr.edu/NGLStationPages/GlobalStationList and the Jet Propulsion Laboratory, California Institute of Technology https://sideshow.jpl.nasa.gov/post/tables/table2.html. A large portion of the compiled earthquake catalog is retrieved from the website of the Canadian Induced Seismicity Collaboration https://www.inducedseismicity.ca/catalogues/. Seismic data were retrieved from the IRIS Data Management Center (IRIS-DMC; https://service.iris.edu/fdsnws/dataselect/1/) using ObsPy (Beyreuther et al., 2010). All these data sources were last accessed in March 2020. The newly compiled earthquake catalog and GNSS station horizontal velocities are presented in Supplementary Tables S1 and S2. The strain tensor parameters were estimated using StrainTool (Dimitrios et al., 2019). All figures were produced using the Generic Mapping Tools (Wessel et al., 2013). O.A.O. would like to thank Ryan Visser, Ramin Dokht for helpful discussions and Desbarats Alexandre (Natural Resources Canada) for mentorship. We appreciate the effort of the Editor, Michael Bostock, and constructive comments received from two anonymous reviewers that helped improve the quality of the submitted manuscript. This project is supported by NRCan LMS Innovation Fund (P-002887.004) and the Environmental Geoscience Program. NRCan contribution 2020xxxx.

References

Adams, J., & Halchuk, S. (2003). Fourth generation seismic hazard maps of Canada: Values for over 650 Canadian localities intended for the 2005 Building Code of Canada, Geol. Surv. Can. Open File, 4459, 155 pp.

Aki, K. (1965). Maximum Likelihood estimation of b in the formula logN=a-bM and its Confidence Limits. *Bull. Earthquake Res Inst.*, Tokyo Univ., 43, 237-239.

Alinia, H. S., Tiampo, K. F., & James, T. S. (2017). GNSS coordinate time series measurements in Ontario and Quebec, Canada. *Journal of Geodesy*, 91(6), 653–683. https://doi.org/10.1007/s00190-016-0987-5

Altamimi, Z., Métivier, L., Rebischung, P., Rouby, H., & Collilieux, X. (2017). ITRF2014 plate motion model. *Geophysical Journal International*, 209(3), 1906–1912. https://doi.org/10.1093/gji/ggx136

Argus, D. F., & Peltier, W. R. (2010). Constraining models of postglacial rebound using space geodesy: A detailed assessment of model ICE-5G (VM2) and its relatives. *Geophysical Journal International*, 181(2), 697–723. https://doi.org/10.1111/j.1365-246X.2010.04562.x

Atkinson, G., Greig, D., & Yenier, E. (2014). Estimation of Moment Magnitude (M) for Small Events (M<4) on Local Networks. *Seismological Research Letters*, 85(5), 1116-1124. https://doi.org/10.1785/0220130180

Audet, P., Currie, C., Schaeffer, A., & Hill, A. (2019). Seismic Evidence for Lithospheric Thinning and Heat in the northern Canadian Cordillera. *Geophysical Research Letters*, 46(8), 4249-4257. https://doi.org/10.1029/2019gl082406

Avouac, J. (2015). From Geodetic Imaging of Seismic and Aseismic Fault Slip to Dynamic Modeling of the Seismic Cycle. *Annual Review of Earth and Planetary Sciences*, 43(1), 233-271. https://doi.org/10.1146/annurev-earth-060614-105302

Bao, X., Eaton, D., & Gu, Y. (2016). Rayleigh wave azimuthally anisotropic phase velocity maps beneath western Canada. *Journal of Geophysical Research: Solid Earth*, 121(3), 1821-1834. https://doi.org/10.1002/2015jb012453

Barani, S., Scafidi, D., & Eva, C. (2010). Strain rates in northwestern Italy from spatially smoothed seismicity. *Journal of Geophysical Research*, 115(B7). https://doi.org/10.1029/2009jb006637

Bertiger, W., Desai, S. D., Haines, B., Harvey, N., Moore, A. W., Owen, S., & Weiss, J. P. (2010). Single receiver phase ambiguity resolution with GNSS data. *Journal of Geodesy*, 84(5), 327–337. https://doi.org/10.1007/s00190-010-0371-9

Beyreuther, M., Barsch, R., Krischer, L., Megies, T., Behr, Y., & Wassermann, J. (2010). ObsPy: A Python Toolbox for Seismology. *Seismological Research Letters*, 81(3), 530-533. https://doi.org/10.1785/gssrl.81.3.530

Bird, P., Jackson, D., Kagan, Y., Kreemer, C., & Stein, R. (2015). GEAR1: A Global Earthquake Activity Rate Model Constructed from Geodetic Strain Rates and Smoothed Seismicity. *Bulletin of The Seismological Society of America*, 105(5), 2538-2554. https://doi.org/10.1785/0120150058

Bird, P., Kreemer, C., & Holt, W. E. (2010). A long-term forecast of shallow seismicity based on the global strain rate map. *Seismological Research Letters*, 81, 184–194. https://doi.org/10.1785/gssrl.81.2.184

Blewitt, G., & Lavallée, D. (2002). Effect of annual signals on geodetic velocity. *Journal of Geophysical Research*, 107(B7), 2145. https://doi.org/10.1029/2001JB000570

Blewitt, G., Hammond, W., & Kreemer, C. (2018). Harnessing the GNSS Data Explosion for Interdisciplinary *Science*. Eos, 99. https://doi.org/10.1029/2018eo104623

Blewitt, G., Kreemer, C., Hammond, W. C., & Gazeaux, J. (2016). MIDAS robust trend estimator for accurate GNSS station velocities without step detection. *Journal of Geophysical Research: Solid Earth*, 121, 2054–2068. https://doi.org/10.1002/2015JB012552

Blewitt, G., Kreemer, C., Hammond, W. C., & Goldfarb, J. M. (2013). Terrestrial reference frame NA12 for crustal deformation studies in North America. *Journal of Geodynamics*, 72, 11–24. https://doi.org/10.1016/j.jog.2013.08.004

Brandes, C., Steffen, H., Steffen, R., & Wu, P. (2015). Intraplate seismicity in northern Central Europe is induced by the last glaciation. *Geology*, 43(7), 611-614. https://doi.org/10.1130/g36710.1

Calais, E., Han, J. Y., DeMets, C., & Nocquet, J. M. (2006). Deformation of the North American plate interior from a decade of continuous GNSS measurements. *Journal of Geophysical Research*, 111, B06402. https://doi.org/10.1029/2005JB004253

Cassidy, J. F., Rogers, G. C., Lamontagne, M., Halchuk, S., and Adams, J. (2010). Canada's earthquakes: the good, the bad, and the ugly. *Geosci. Can.,* 37, 1–16.

Cassidy, J.F., & Bent, A.L., (1993). Source parameters of the 29 May and 5 June, 1940, Richardson Mountains, Yukon Territory, earthquakes: *Bulletin of the Seismological Society of America*, v. 83, 636-659.

Chen, K., Xu, W., Mai, P., Gao, H., Zhang, L., & Ding, X. (2018). The 2017 Mw 7.3 Sarpol Zahāb Earthquake, Iran: A compact blind shallow-dipping thrust event in the mountain front fault basement. *Tectonophysics*, 747-748, 108-114. https://doi.org/10.1016/j.tecto.2018.09.015

Chen, Y., Gu, Y., Currie, C., Johnston, S., Hung, S., Schaeffer, A., & Audet, P. (2019). Seismic evidence for a mantle suture and implications for the origin of the Canadian Cordillera. *Nature Communications*, 10(1). https://doi.org/10.1038/s41467-019-09804-8

Clark, J., Mitrovica, J., & Latychev, K. (2019). Glacial isostatic adjustment in central Cascadia: Insights from three-dimensional Earth modeling. *Geology*, 47(4), 295-298. https://doi.org/10.1130/g45566.1

Clarke, P., Davies, R., England, P., Parsons, B., Billiris, H., & Paradissis, D. et al. (1997). Geodetic estimate of seismic hazard in the Gulf of Korinthos. *Geophysical Research Letters*, 24(11), 1303-1306. https://doi.org/10.1029/97gl01042

Cui, L., & Atkinson, G. (2016). Spatiotemporal Variations in the Completeness Magnitude of the Composite Alberta Seismicity Catalog (CASC). *Seismological Research Letters*, 87(4), 853-863. https://doi.org/10.1785/0220150268

D'Agostino, N. (2014). Complete seismic release of tectonic strain and earthquake recurrence in the Apennines (Italy). *Geophysical Research Letters*, 41(4), 1155-1162. https://doi.org/10.1002/2014gl059230

Déprez, A., Doubre, C., Masson, F., & Ulrich, P. (2013). Seismic and aseismic deformation along the East African Rift System from a reanalysis of the GNSS velocity field of Africa. *Geophysical Journal International*, 193(3), 1353-1369. https://doi.org/10.1093/gji/ggt085

Dimitrios, G., Papanikolaou, X., Ganas, A., & Paradissis, D. (2019). StrainTool: A software package to estimate strain tensor parameters (Version v1.0). *Zenodo*. http://doi.org/10.5281/zenodo.3266398

Dokht, R., Kao, H., Visser, R., & Smith, B. (2019). Seismic Event and Phase Detection Using Time–Frequency Representation and Convolutional Neural Networks. *Seismological Research Letters*, 90(2A), 481-490. https://doi.org/10.1785/0220180308

Dyke, A.S., (2004). An outline of North American deglaciation with emphasis on central and northern *Canada. Dev. Quat. Sci.,* 2, 373e424.

Efron, B. (1979). Bootstrap Methods: Another Look at the Jackknife. *The Annals of Statistics*, 7(1), 1-26. https://doi.org/10.1214/aos/1176344552

Elliott, J., Larsen, C., Freymueller, J., & Motyka, R. (2010). Tectonic block motion and glacial isostatic adjustment in southeast Alaska and adjacent Canada constrained by GPS measurements. *Journal of Geophysical Research*, 115(B9). https://doi.org/10.1029/2009jb007139

England, P. (1997). Active Deformation of Asia: From Kinematics to Dynamics. *Science*, 278(5338), 647-650. https://doi.org/10.1126/science.278.5338.647

Estève, C., Audet, P., Schaeffer, A., Schutt, D., Aster, R., & Cubley, J. (2020). The Upper Mantle Structure of Northwestern Canada From Teleseismic Body Wave Tomography. *Journal of Geophysical Research: Solid Earth*, 125(2). https://doi.org/10.1029/2019jb018837

Fereidoni, A., and L. Cui (2015). Composite Alberta Seismicity Catalog: CASC2014-x, http://www.inducedseismicity.ca/wp-content/uploads/2015/01/Composite-Alberta-Seismicity-Catalog3.pdf (last accessed March 2020).

Fereidoni, A., Atkinson, G., Macias, M., & Goda, K. (2012). CCSC: A Composite Seismicity Catalog for Earthquake Hazard Assessment in Major Canadian Cities. *Seismological Research Letters*, 83(1), 179-189. https://doi.org/10.1785/gssrl.83.1.179

Field, E., Jackson, D. D., & Dolan, J. F. (1999). A mutually consistent seismic hazard source model for southern California, *Bulletin of The Seismological Society of America*, 89, 559–578.

Gao, D., K. Wang, E. E. Davis, Y. Jiang,T. L. Insua, and J. He (2017), Thermal state of the Explorer segment of the Cascadia subduction zone: Implications for seismic and tsunami hazards, *Geochemistry, Geophysics, Geosystems*,18, 1569–1579, doi:10.1002/2017GC006838.

George, N. V., Tiampo, K. F., Sahu, S. S., Mazzotti, S., Mansinha, L., & Panda, G. (2012). Identification of glacial isostatic adjustment in eastern Canada using S transform filtering of GNSS observations. *Pure and Applied Geophysics*, 169(8), 1507–1517. https://doi.org/10.1007/s00024-011-0404-1

George, N., Tiampo, K., Sahu, S., Mazzotti, S., Mansinha, L., & Panda, G. (2011). Identification of Glacial Isostatic Adjustment in Eastern Canada Using S Transform Filtering of GNSS Observations. *Pure and Applied Geophysics*, 169(8), 1507-1517. https://doi.org/10.1007/s00024-011-0404-1

Ghofrani, H., & Atkinson, G. (2016). A preliminary statistical model for hydraulic fracture-induced seismicity in the Western Canada Sedimentary Basin. *Geophysical Research Letters*, 43(19), 10,164-10,172. https://doi.org/10.1002/2016gl070042

González-Ortega, J., González-García, J., & Sandwell, D. (2018). Interseismic Velocity Field and Seismic Moment Release in Northern Baja California, Mexico. *Seismological Research Letters*, 89(2A), 526-533. https://doi.org/10.1785/0220170133

Goudarzi, M., Cocard, M., & Santerre, R. (2016). Present-Day 3D Velocity Field of Eastern North America Based on Continuous GNSS Observations. *Pure and Applied Geophysics*, 173(7), 2387-2412. https://doi.org/10.1007/s00024-016-1270-7

Grunewald, E., & Stein, R. (2006). A new 1649-1884 catalog of destructive earthquakes near Tokyo and implications for the long-term seismic process. *Journal Of Geophysical Research: Solid Earth*, 111(B12), n/a-n/a. https://doi.org/10.1029/2005jb004059

Guest, B., Stockli, D., Grove, M., Axen, G., Lam, P., & Hassanzadeh, J. (2006). Thermal histories from the central Alborz Mountains, northern Iran: Implications for the spatial and temporal distribution of deformation in northern Iran. *Geological Society of America Bulletin*, 118(11-12), 1507-1521. https://doi.org/10.1130/b25819.1

Gutenberg B., & Richter, C.F., (1944). Frequency of earthquakes in California. *Bulletin of the Seismological Society of America*, v. 3, 185-188.

Halchuk, S. C., Adams, J. E., & Allen, T. I. (2015). Fifth Generation Seismic Hazard Model for Canada: Grid values of mean hazard to be used with the 2015 National Building Code of Canada. *Geological Survey of Canada Open-File Report*, 7893, 26. https://doi.org/10.4095/297378

Hanks, T., & Kanamori, H. (1979). A moment magnitude scale. *Journal of Geophysical Research*, 84(B5), 2348. https://doi.org/10.1029/jb084ib05p02348

Henton, J. A., Craymer, M. R., Ferland, R., Dragert, H., Mazzotti, S., & Forbes, D. L. (2006). Crustal motion and deformation monitoring of the Canadian landmass. *Geomatica*, 60(2), 173–191.

Hussain, E., Wright, T., Walters, R., Bekaert, D., Lloyd, R., & Hooper, A. (2018). Constant strain accumulation rate between major earthquakes on the North Anatolian Fault. *Nature Communications*, 9(1). https://doi.org/10.1038/s41467-018-03739-2

Hyndman, R., & Weichert, D. (1983). Seismicity and rates of relative motion on the plate boundaries of Western North America. *Geophysical Journal International*, 72(1), 59-82. https://doi.org/10.1111/j.1365-246x.1983.tb02804.x

James, T., Clague, J., Wang, K., & Hutchinson, I. (2000). Postglacial rebound at the northern Cascadia subduction zone. *Quaternary Science Reviews*, 19(14-15), 1527-1541. https://doi.org/10.1016/s0277-3791(00)00076-7

Jenny, S., Goes, S., Giardini, D., & Kahle, H. (2004). Earthquake recurrence parameters from seismic and geodetic strain rates in the eastern Mediterranean*. Geophysical Journal International*, 157(3), 1331-1347. https://doi.org/10.1111/j.1365-246x.2004.02261.x

Jiang, Y., Wdowinski, S., Dixon, T. H., Hackl, M., Protti, M., & Gonzalez, V. (2012). Slow slip events in Costa Rica detected by continuous GNSS observations, 2002-2011. *Geochemistry, Geophysics, Geosystems*, 13, Q04006. https://doi.org/10.1029/2012GC004058

Kagan, Y. (1999). Universality of the Seismic Moment-frequency Relation. *Pure and Applied Geophysics*, 155(2-4), 537-573. https://doi.org/10.1007/s000240050277

Kagan, Y. (2002). Seismic moment distribution revisited: II. Moment conservation principle. *Geophysical Journal International*, 149(3), 731-754. https://doi.org/10.1046/j.1365-246x.2002.01671.x

Kagan, Y., & Jackson, D. (2013). Tohoku Earthquake: A Surprise?. *Bulletin of The Seismological Society of America*, 103(2B), 1181-1194. https://doi.org/10.1785/0120120110

Kao, H., Hyndman, R., Jiang, Y., Visser, R., Smith, B., & Babaie Mahani, A. et al. (2018). Induced Seismicity in Western Canada Linked to Tectonic Strain Rate: Implications for Regional Seismic Hazard. *Geophysical Research Letters*, 45(20). https://doi.org/10.1029/2018gl079288

Kao, H., Behr, Y., Currie, C., Hyndman, R., Townend, J., & Lin, F. et al. (2013). Ambient seismic noise tomography of Canada and adjacent regions: Part I. Crustal structures. *Journal of Geophysical Research: Solid Earth*, 118(11), 5865-5887. https://doi.org/10.1002/2013jb010535

Keiding, M., Kreemer, C., Lindholm, C., Gradmann, S., Olesen, O., & Kierulf, H. (2015). A comparison of strain rates and seismicity for Fennoscandia: depth dependency of deformation from glacial isostatic adjustment. *Geophysical Journal International*, 202(2), 1021-1028. https://doi.org/10.1093/gji/ggv207

King, M., Altamimi, Z., Boehm, J., Bos, M., Dach, R., & Elosegui, P. et al. (2010). Improved Constraints on Models of Glacial Isostatic Adjustment: A Review of the Contribution of Ground-Based Geodetic Observations. *Surveys in Geophysics*, 31(5), 465-507. https://doi.org/10.1007/s10712-010-9100-4

Kostrov, B. V. (1974). Seismic moment and energy of earthquakes, and seismic flow of rock, *Earth Phys*., 1, 23–40.

Kreemer, C., Blewitt, G., & Klein, E. C. (2014). A geodetic plate motion and global strain rate model. *Geochemistry, Geophysics, Geosystems*, 15, 3849–3889. https://doi.org/10.1002/2014GC005407

Kreemer, C., Hammond, W. C., & Blewitt, G. (2018). A robust estimation of the 3-D intraplate deformation of the North American plate from GNSS. *Journal of Geophysical Research: Solid Earth*, 123, 4388–4412. https://doi.org/10.1029/2017JB015257

Kreemer, C., Hammond, W., & Blewitt, G. (2018). A Robust Estimation of the 3-D Intraplate Deformation of the North American Plate From GNSS. *Journal of Geophysical Research: Solid Earth*, 123(5), 4388-4412. https://doi.org/10.1029/2017jb015257

Kreemer, C., Holt, W. E., & Haines, A. J. (2002). The global moment rate distribution within plate boundary zones. In S. Stein & J. T. Freymueller (Eds.), Plate boundary zones (pp. 173–190). Washington, DC: American Geophysical Union.

Kreemer, C., Holt, W., Goes, S., & Govers, R. (2000). Active deformation in eastern Indonesia and the Philippines from GNSS and seismicity data. *Journal of Geophysical Research: Solid Earth*, 105(B1), 663-680. https://doi.org/10.1029/1999jb900356

Kuchar, J., Milne, G., & Latychev, K. (2019). The importance of lateral Earth structure for North American glacial isostatic adjustment. *Earth and Planetary Science Letters*, 512, 236-245. https://doi.org/10.1016/j.epsl.2019.01.046

Lambert, A., Courtier, N., Sasagawa, G., Klopping, F., Winester, D., James, T., & Liard, J. (2001). New constraints on Laurentide postglacial rebound from absolute gravity measurements. *Geophysical Research Letters*, 28(10), 2109-2112. https://doi.org/10.1029/2000gl012611

Lamontagne, M., 1999. Rheological and geological constraints on the earthquake distribution in the Charlevoix Seismic Zone, Quebec, Canada (Ph.D. Thesis). Carleton University, Canada.

Lamothe, P., Santerre, R., Cocard, M., & Mazzotti, S. (2010). A crustal deformation study of the Charlevoix seismic zone in Quebec. *Geomatica*, 64(3), 61–67.

Larsen, C., Motyka, R., Freymueller, J., Echelmeyer, K., & Ivins, E. (2005). Rapid viscoelastic uplift in southeast Alaska caused by post-Little Ice Age glacial retreat. *Earth and Planetary Science Letters*, 237(3-4), 548-560. https://doi.org/10.1016/j.epsl.2005.06.032

Lavoie, C., Allard, M., & Duhamel, D. (2012). Deglaciation landforms and C-14 chronology of the Lac Guillaume-Delisle area, eastern Hudson Bay: A report on field evidence. *Geomorphology*, 159-160, 142-155. https://doi.org/10.1016/j.geomorph.2012.03.015

Lemieux, Y., Tremblay, A., & Lavoie, D. (2003). Structural analysis of supracrustal faults in the Charlevoix area, Quebec: relation to impact cratering and the St-Laurent fault system. *Canadian Journal of Earth Sciences*, 40(2), 221-235. https://doi.org/10.1139/e02-046

Li, S., Wang, K., Wang, Y., Jiang, Y., & Dosso, S. (2018). Geodetically Inferred Locking State of the Cascadia Megathrust Based on a Viscoelastic Earth Model. *Journal of Geophysical Research: Solid Earth*, 123(9), 8056-8072. https://doi.org/10.1029/2018jb015620

Masson, F., Chéry, J., Hatzfeld, D., Martinod, J., Vernant, P., Tavakoli, F., & Ghafory-Ashtiani, M. (2004). Seismic versus aseismic deformation in Iran inferred from earthquakes and geodetic data. *Geophysical Journal International*, 160(1), 217-226. https://doi.org/10.1111/j.1365-246x.2004.02465.x

Masson, F., Djamour, Y., Van Gorp, S., Chéry, J., Tatar, M., & Tavakoli, F. et al. (2006). Extension in NW Iran driven by the motion of the South Caspian Basin. *Earth and Planetary Science Letters*, 252(1-2), 180-188. https://doi.org/10.1016/j.epsl.2006.09.038

Mazzotti, S., & Townend, J. (2010). State of stress in central and eastern North American seismic zones. *Lithosphere*, 2(2), 76-83. https://doi.org/10.1130/l65.1

Mazzotti, S., Hyndman, R., Flück, P., Smith, A., & Schmidt, M. (2003). Distribution of the Pacific/North America motion in the Queen Charlotte Islands-S. Alaska plate boundary zone. *Geophysical Research Letters*, 30(14). https://doi.org/10.1029/2003gl017586

Mazzotti, S., James, T., Henton, J., & Adams, J. (2005). GNSS crustal strain, postglacial rebound, and seismic hazard in eastern North America: The Saint Lawrence valley example. *Journal of Geophysical Research: Solid Earth*, 110(B11). https://doi.org/10.1029/2004jb003590

Mazzotti, S., Lambert, A., Henton, J., James, T., & Courtier, N. (2011). Absolute gravity calibration of GNSS velocities and glacial isostatic adjustment in mid-continent North America. *Geophysical Research Letters*, 38(24), n/a-n/a. https://doi.org/10.1029/2011gl049846

McCaffrey, R., King, R., Payne, S., & Lancaster, M. (2013). Active tectonics of northwestern U.S. inferred from GPS-derived surface velocities. *Journal of Geophysical Research: Solid Earth*, 118(2), 709-723. https://doi.org/10.1029/2012jb009473

McLellan, M., Schaeffer, A., & Audet, P. (2018). Structure and fabric of the crust and uppermost mantle in the northern Canadian Cordillera from Rayleigh-wave tomography. *Tectonophysics*, 724-725, 28-41. https://doi.org/10.1016/j.tecto.2018.01.011

Mey, J., Scherler, D., Wickert, A., Egholm, D., Tesauro, M., Schildgen, T., & Strecker, M. (2016). Glacial isostatic uplift of the European Alps. *Nature Communications*, 7(1). https://doi.org/10.1038/ncomms13382

Middleton, T., Parsons, B., & Walker, R. (2017). Comparison of seismic and geodetic strain rates at the margins of the Ordos Plateau, northern China. *Geophysical Journal International*, 212(2), 988-1009. https://doi.org/10.1093/gji/ggx446

Mignan, A., and Woessner, J. (2012). Estimating the magnitude of completeness for earthquake catalogs. Community Online Resource for Statistical Seismicity Analysis. http://dx.doi.org/10.5078/corssa-00180805

Mignan, A., Werner, M., Wiemer, S., Chen, C., & Wu, Y. (2011). Bayesian Estimation of the Spatially Varying Completeness Magnitude of Earthquake Catalogs. *Bulletin of The Seismological Society of America*, 101(3), 1371-1385. https://doi.org/10.1785/0120100223

Mitrovica, J., Tamisiea, M., Davis, J., & Milne, G. (2001). Recent mass balance of polar ice sheets inferred from patterns of global sea-level change. *Nature*, 409(6823), 1026-1029. https://doi.org/10.1038/35059054

Molnar, P. (1979). Earthquake recurrence intervals and plate tectonics. *Bulletin of the Seismological Society of America*, 69(1), 115–133.

Moratto, L., Saraò, A., & Priolo, E. (2017). Moment Magnitude (Mw) Estimation of Weak Seismicity in Northeastern Italy. *Seismological Research Letters*, 88(6), 1455-1464. https://doi.org/10.1785/0220170063

Neely, J., Stein, S., Merino, M., & Adams, J. (2018). Have we seen the largest earthquakes in eastern North America?. *Physics of The Earth and Planetary Interiors*, 284, 17-27. https://doi.org/10.1016/j.pepi.2018.09.005

Nield, G., Barletta, V., Bordoni, A., King, M., Whitehouse, P., & Clarke, P. et al. (2014). Rapid bedrock uplift in the Antarctic Peninsula explained by viscoelastic response to recent ice unloading. *Earth and Planetary Science Letters*, 397, 32-41. https://doi.org/10.1016/j.epsl.2014.04.019

Nield, G., Whitehouse, P., van der Wal, W., Blank, B., O'Donnell, J., & Stuart, G. (2018). The impact of lateral variations in lithospheric thickness on glacial isostatic adjustment in West Antarctica. *Geophysical Journal International*, 214(2), 811-824. https://doi.org/10.1093/gji/ggy158

Novakovic, M., & Atkinson, G. (2015). Preliminary Evaluation of Ground Motions from Earthquakes in Alberta. *Seismological Research Letters*, 86(4), 1086-1095. https://doi.org/10.1785/0220150059

Palano, M., Imprescia, P., Agnon, A., & Gresta, S. (2017). An improved evaluation of the seismic/geodetic deformation-rate ratio for the Zagros Fold-and-Thrust collisional belt. *Geophysical Journal International*, 213(1), 194-209. https://doi.org/10.1093/gji/ggx524

Pancha, A. (2006). Comparison of Seismic and Geodetic Scalar Moment Rates across the Basin and Range Province. *Bulletin of The Seismological Society of America*, 96(1), 11-32. https://doi.org/10.1785/0120040166

Pancha, A. (2006). Comparison of Seismic and Geodetic Scalar Moment Rates across the Basin and Range Province. *Bulletin of The Seismological Society of America*, 96(1), 11-32. https://doi.org/10.1785/0120040166

Park, K. (2002). Investigation of glacial isostatic adjustment in the northeast U.S. using GNSS measurements. *Geophysical Research Letters*, 29(11). https://doi.org/10.1029/2001gl013782

Peltier, W. (1994). Ice Age Paleotopography. *Science*, 265(5169), 195-201. https://doi.org/10.1126/science.265.5169.195

Peltier, W. (2002). Global glacial isostatic adjustment: palaeogeodetic and space-geodetic tests of the ICE-4G (VM2) model. *Journal of Quaternary Science*, 17(5-6), 491-510. https://doi.org/10.1002/jqs.713

Peltier, W. R., Argus, D. F., & Drummond, R. (2015). Space geodesy constrains ice age terminal deglaciation: The global ICE-6G_C (VM5a) model. *Journal of Geophysical Research; Solid Earth*, 120, 450–487. https://doi.org/10.1002/2014JB011176

Peltier, W. R., Argus, D. F., & Drummond, R. (2018). Comment on the paper by Purcell et al. (2016) entitled "An assessment of the ICE-6G_C (VM5a) glacial isostatic adjustment model". *Journal of Geophysical Research: Solid Earth*, 123, 2019–2028. https://doi.org/10.1002/2016JB013844

Petersen, M. D., Mueller, C. S., Moschetti, M. P., Hoover, S. M., Llenos, A. L., Ellsworth, W. L., Michael, A. J., Rubinstein, J. L., McGarr, A. F., & Rukstales, K. S. (2016). One-year seismic hazard forecast for the Central and Eastern United States from induced and natural earthquakes, U.S. Geol. Surv. Open File Rep. 2016–1035, 52, doi:10.3133/ofr20161035

Rebischung, P., Griffiths, J., Ray, J., Schmid, R., Collilieux, X., & Garayt, B. (2012). IGS08: The IGS realization of ITRF2008. *GNSS Solutions*, 16(4), 483–494. https://doi.org/10.1007/s10291-011-0248-2

Reid, H. F. (1910), The California Earthquake of April 18, 1906. Volume II. The Mechanics of the Earthquake, Carnegie Institution of Washington, Washington, D. C.

Riddihough, R.P. & Hyndman, R.D. (1991). Modern plate tectonic regime of the continental margin of Western Canada, in Geology of the Cordilleran Orogen in Canada, H. Gabrielse and C.J. Yorath (eds.), Geol. Surv. Canada, Geology of Canada, No. 4, (also Geol. Soc. Am., The Geology of North America, V. G2).

Riguzzi, F., Crespi, M., Devoti, R., Doglioni, C., Pietrantonio, G., & Pisani, A. R. (2012). Geodetic strain rate and earthquake size: New clues for seismic hazard studies. *Physics of the Earth and Planetary Interiors*, 206, 67–75.

Ristau, J. P. (2004). Seismotectonics of western Canada from regional moment tensor analysis, Ph.D. Thesis, University of Victoria, Victoria, Canada, 209 pp.

Ristau, J., Rogers, G. C., & Cassidy, J. F. (2005). Moment magnitude-local magnitude calibration for earthquakes in western Canada, *Bulletin of the Seismological Society of America*, 95, 1994-2000.

Rong, Y., Jackson, D., Magistrale, H., & Goldfinger, C. (2014). Magnitude Limits of Subduction Zone Earthquakes. *Bulletin of The Seismological Society Of America*, 104(5), 2359-2377. https://doi.org/10.1785/0120130287

Rontogianni, S. (2010). Comparison of geodetic and seismic strain rates in Greece by using a uniform processing approach to campaign GNSS measurements over the interval 1994–2000. *Journal of Geodynamics*, 50(5), 381-399. https://doi.org/10.1016/j.jog.2010.04.008

Savage, J. C., & Simpson, R. W. (1997). Surface strain accumulation and the seismic moment tensor, *Bulletin of the Seismological Society of America*, 87, 1345–1353.

Sella, G. F., Stein, S., Dixon, T. H., Craymer, M., James, T. S., Mazzotti, S., & Dokka, R. K. (2007). Observation of glacial isostatic adjustment in “stable” North America with GNSS. *Geophysical Research Letters*, 34, L02306. https://doi.org/10.1029/2006GL027081

Sella, G.F., Stein, S., Wdowinski, S., Dixon, T.H., Craymer, M.R., & James, T.S. (2004). Direct constraints on GIA motion in North America using GNSS, in: AGU Spring Meeting Abstracts. p. 3.

Sen, P. (1968). Estimates of the Regression Coefficient Based on Kendall's Tau. *Journal of The American Statistical Association*, 63(324), 1379-1389. https://doi.org/10.1080/01621459.1968.10480934

Shen, Z., Wang, M., Zeng, Y., & Wang, F. (2015). Optimal Interpolation of Spatially Discretized Geodetic Data. *Bulletin of The Seismological Society of America*, 105(4), 2117-2127. https://doi.org/10.1785/0120140247

Snay, R., Freymueller, J., Craymer, M., Pearson, C., & Saleh, J. (2016). Modeling 3-D crustal velocities in the United States and Canada. *Journal of Geophysical Research: Solid Earth*, 121(7), 5365-5388. https://doi.org/10.1002/2016jb012884

Steffen, R., Wu, P., Steffen, H., & Eaton, D. W. (2014). The effect of Earth rheology and ice-sheet size on fault slip and magnitude of postglacial earthquakes. *Earth and Planetary Science Letters*, 388, 71–80.

Stern, V. H., Schultz, R. J., Shen, L., Gu, Y. J., & Eaton, D. W. (2013). Alberta earthquake catalogue, version 1.0: September 2006 through December 2010, *Alberta Geological Survey Open File Report*, 2013-15, 36 pp

Tan, F., Kao, H., Nissen, E., & Eaton, D. (2019). Seismicity-Scanning Based on Navigated Automatic Phase-Picking. *Journal of Geophysical Research: Solid Earth*, 124(4), 3802-3818. https://doi.org/10.1029/2018jb017050

Tarayoun, A., Mazzotti, S., Craymer, M., & Henton, J. (2018). Structural Inheritance Control on Intraplate Present-Day Deformation: GNSS Strain Rate Variations in the Saint Lawrence Valley, Eastern Canada. *Journal Of Geophysical Research: Solid Earth,*123. https://doi.org/10.1029/2017jb015417

Theil, H. (1950). A rank-invariant method of linear and polynomial regression analysis, *Indag. Math*., 12, 85–91.

Tiampo, K., Mazzotti, S., & James, T. (2011). Analysis of GNSS Measurements in Eastern Canada Using Principal Component Analysis. *Pure and Applied Geophysics*, 169(8), 1483-1506. https://doi.org/10.1007/s00024-011-0420-1

Tushingham, A., & Peltier, W. (1991). Ice-3G: A new global model of Late Pleistocene deglaciation based upon geophysical predictions of post-glacial relative sea level change. *Journal of Geophysical Research: Solid Earth*, 96(B3), 4497-4523. https://doi.org/10.1029/90jb01583

van der Wal, W., Braun, A., Wu, P., & Sideris, M. (2009). Prediction of decadal slope changes in Canada by glacial isostatic adjustment modelling. *Canadian Journal of Earth Sciences*, 46(8), 587-595. https://doi.org/10.1139/e09-044

Visser, R., Smith, B., Kao, H., Babaie Mahani, A., Hutchinson, J., & McKay, J. E. (2017). A comprehensive earthquake catalogue for northeastern British Columbia and western Alberta, 2014–2016. *Geological Survey of Canada Open-File Report*, 8335, 27. https://doi.org/10.4095/306292

Wahr, J., DaZhong, H., & Trupin, A. (1995). Predictions of vertical uplift caused by changing polar ice volumes on a viscoelastic Earth. *Geophysical Research Letters*, 22(8), 977-980. https://doi.org/10.1029/94gl02840

Walpersdorf, A., Hatzfeld, D., Nankali, H., Tavakoli, F., Nilforoushan, F., & Tatar, M. et al. (2006). Difference in the GNSS deformation pattern of North and Central Zagros (Iran). *Geophysical Journal International*, 167(3), 1077-1088. https://doi.org/10.1111/j.1365-246x.2006.03147.x

Wang, K., Wells, R., Mazzotti, S., Hyndman, R., & Sagiya, T. (2003). A revised dislocation model of interseismic deformation of the Cascadia subduction zone. *Journal of Geophysical Research: Solid Earth*, 108(B1). https://doi.org/10.1029/2001jb001227

Ward, S. (1998a). On the consistency of earthquake moment rates, geological fault data, and space geodetic strain: the United States. *Geophysical Journal International*, 134(1), 172-186. https://doi.org/10.1046/j.1365-246x.1998.00556.x

Ward, S. (1998b). On the consistency of earthquake moment release and space geodetic strain rates: Europe. *Geophysical Journal International*, 135(3), 1011-1018. https://doi.org/10.1046/j.1365-246x.1998.t01-2-00658.x

Weichert, D. H. (1980). Estimation of the earthquake recurrence parameters from unequal observation periods for different magnitudes, *Bulletin of the Seismological Society of America*, 70, 1337-1346.

Weldon, R., Scharer, K., Fumal, T., & Biasi, G. (2004). Wrightwood and the earthquake cycle: What a long recurrence record tells us about how faults work. *GSA Today*, 14(9), 4. https://doi.org/10.1130/1052-5173(2004)014<4:watecw>2.0.co;2

Wessel, P., Smith, W., Scharroo, R., Luis, J., & Wobbe, F. (2013). Generic Mapping Tools: Improved Version Released. *Eos, Transactions American Geophysical Union*, 94(45), 409-410. https://doi.org/10.1002/2013eo450001

Wiemer, S. (2000). Minimum Magnitude of Completeness in Earthquake Catalogs: Examples from Alaska, the Western United States, and Japan. *Bulletin of the Seismological Society of America*, 90(4), 859-869. https://doi.org/10.1785/0119990114

Wu, L., Gu, Y., Chen, Y., & Liang, H. (2019). Shear Wave Splitting Discloses Two Episodes of Collision-Related Convergence in Western North America. *Journal of Geophysical Research: Solid Earth*, 124(3), 2990-3010. https://doi.org/10.1029/2018jb016352

Yousefi, M., Milne, G., Li, S., Wang, K.,& Bartholet, A. (2020). Constraining interseismic deformation of the Cascadia subduction zone: New insights from estimates of vertical land motion over different timescales. *Journal of Geophysical Research: Solid Earth*, 125, e2019JB018248. https://doi.org/10.1029/2019JB018248

Zeng, Y., Petersen, M. D., & Shen, Z. K. (2018). Earthquake potential in California-Nevada implied by correlation of strain rate and seismicity. *Geophysical Research Letters*, 45(4), 1778–1785. https://doi.org/10.1002/2017GL075967

Zumberge, J. F., Heflin, M. B., Jefferson, D. C., Watkins, M. M., & Webb, F. H. (1997). Precise point positioning for the efficient and robust analysis of GNSS data from large networks. *Journal of Geophysical Research*, 102(B3), 5005–5017. https://doi.org/10.1029/96JB03860